Genesis of Diamond Dust, Ice Fog and Thick Cloud Episodes observed and modelled above Dome C, Antarctica

Philippe Ricaud[1], Eric Bazile[1], Massimo del Guasta[2], Christian Lanconelli[3,4], Paolo Grigioni[5], Achraf Mahjoub[1]

[1]Météo-France/CNRM, CNRS UMR 3589, 42 avenue Gaspard Coriolis, 31057 Toulouse, France

[2]INO-CNR, Via Madonna del Piano 10, 50019, Sesto Fiorentino, Italy

[3]Institute of Atmospheric Sciences and Climate (ISAC), Consiglio Nazionale delle Ricerche, via Gobetti 101, 40129 Bologna, Italy;

[4]Now at Joint Research Center, Institute for Environment and Sustainability (IES), Land Resource Management Unit (H05), via Fermi, 21027 Ispra (VA), Italy

[5]ENEA, Lungotevere Thaon di Revel, 76-00196 Roma, Italy

Version V11, 30 January 2017

Revision – R1

Submitted to: *Atmospheric Chemistry and Physics Discussions*

Abstract

Episodes of thick cloud and diamond dust/ice fog were observed during 15 March to 8 April 2011 and 4 to 5 March 2013 in the atmosphere above Dome C (Concordia station, Antarctica, 75°06'S, 123°21'E, 3233 m amsl). The objectives of the paper are mainly to investigate the processes that cause these episodes based on observations and to verify whether operational models can evaluate them. The measurements were obtained from the following instruments: 1) A ground-based microwave radiometer (HAMSTRAD, H_2O Antarctica Microwave Stratospheric and Tropospheric Radiometers) installed at Dome C that provided vertical profiles of tropospheric temperature and absolute humidity every 7 minutes. 2) Daily radiosoundings launched at 12:00 UTC at Dome C. 3) A tropospheric aerosol Lidar that provides aerosol depolarization ratio along the vertical at Dome C. 4) Down- and upward short- and longwave radiations as provided by the Baseline Surface Radiation Network (BSRN) facilities. 5) An ICE-CAMERA to detect at an hourly rate the size of the ice crystal grains deposited at the surface of the camera. 6) Space-borne aerosol depolarization ratio from the Cloud-Aerosol Lidar with Orthogonal Polarization (CALIOP) Lidar aboard the Cloud-Aerosol Lidar and Infrared Pathfinder Satellite Observation (CALIPSO) platform along orbits close to the Dome C station. The time evolution of the atmosphere has also been evaluated by considering the outputs from the meso-scale AROME and the global-scale ARPEGE meteorological models. Thick clouds are detected during the warm and wet periods (24-26 March 2011 and 4 March 2013) with high depolarization ratios (greater than 30%) from the surface to 5-7 km above the ground associated with precipitation of ice particles and the presence of a supercooled liquid water (depolarization less than 10%) clouds. Diamond dust and/or ice fog are detected during the cold and dry periods (5 April 2011 and 5 March 2013) with high depolarization ratios (greater than 30%) in the planetary boundary layer to a maximum altitude of 100-300 m above the ground with little trace of precipitation. Considering

45   5-day back trajectories, we show that the thick-cloud episodes are attributed to air masses with

46   an oceanic origin whilst the diamond dust/ice fog episodes are attributed to air masses with

47   continental origins. Although operational models can reproduce thick cloud episodes in the free

48   troposphere, they cannot evaluate the diamond dust/ice fog episodes in the planetary boundary

49   layer because they require to use more sophisticated cloud and aerosol microphysics schemes.

1. Introduction

The impact of global warming has become obvious in high latitude regions, particularly in the Arctic region, where melting ice and softening tundra are causing profound changes. The environmental response of the Arctic is characteristically different from that of the Antarctic because of differences in planetary geography and energy circulation. Over the past 50 years, the west coast of the Antarctic Peninsula has been one of the most rapidly warming parts of the planet. This warming is not only restricted to the land but can also be noted in the Southern Ocean. For example, the warming of the Antarctic winter troposphere is more important than anywhere on Earth with a rate of 0.5 to 0.7°C per decade measured over the last thirty years (Turner et al., 2006). In Antarctica, the polar vortex is more intense, is colder and lasts longer than in Arctic. The role of the Antarctic ice is important because it is one of the key parameters in the regulation of air temperature near the surface. During the austral winter, in the absence of solar radiation, the surface cools via infrared radiation emitted towards a very cold and very dry atmosphere. In the austral summer, the absorption of solar radiation at shorter wavelength produces a diurnal cycle and warms the surface while heating is limited by a high albedo (Pirazzini, 2004; Hudson et al., 2006).

Changes in the abundance of water vapour (H_2O) influence directly (and indirectly via clouds) the Earth's radiation budget and therefore affect climate change (Brasseur et al., 1999) because H_2O is the main greenhouse gas that emits and absorbs in the infrared domain. With an average altitude of 2500 m above sea level, the Antarctic Plateau is one of the coldest and driest places of the planet, for instance with temperature less than -80 °C and integrated water vapor amount less than 0.5 mm in winter at the Dome C station (e.g., Tomasi et al., 2012). For these reasons, numerous studies focused on climate change (e.g., Hines et al., 2004), processes in the atmospheric boundary layer (e.g., Argentini et al, 2005), reactive species interacting with the snow (e.g., Davis et al., 2001) and astronomical site quality (e.g., Tremblin et al, 2011).

Clouds play an important role in the radiation budget of the Earth. Since they have large spatial, seasonal and diurnal variability and they are poorly represented in climate models, large differences are obtained by climate models when assessing the strength and the direction of the cloud feedback on the Earth radiation balance (Dufresne and Bony, 2008). The interconnections between the Antarctic, the middle latitudes and the tropics show that Antarctic clouds are an important part of the global climate system (Lubin et al., 1998). Based on observations from CloudSat and Cloud-Aerosol Lidar and Infrared Pathfinder Satellite Observation (CALIPSO) satellites over the period 2006-2010 (Adhikari et al., 2012), it is found that the Antarctic Plateau has the lowest cloud occurrence of the Antarctic continent (<30%). The continental region of the Antarctic Plateau experiences cloud about 30% of the time at altitudes below 3 km and less than 10% of the time above 5 km. Cloud occurrence over the western continental region is about 50% below 3 km and about 30% from the surface up to 8 km. Furthermore, whatever the season considered, it is shown that multilayer clouds occur over Antarctica.

The Dome C station (Concordia) in Antarctica (75°06'S, 123°21'E, 3233 m above mean sea level) is operated jointly by the French Polar Institute Paul-Emile Victor (IPEV) and the Italian Institute Programma Nazionale Ricerche in Antartide (PNRA). The site is located on the Antarctic plateau with 24 hours a day in summer and 24 hours of night in winter, a climatological temperature between -40 °C and -20 °C in summer and -80° C and -60 °C in winter (Tomasi et al., 2006). Situated on top of a dome, there is no katabatic wind as in the case of the costal station of Dumont d'Urville (66°S, 140°E, 0 m above sea level) since the average wind rarely exceeds 5 m s^{-1} throughout the year. When the temperature drops, water may precipitate and light ice crystals may be suspended in the air with little trace of precipitation producing a phenomenon referred to as diamond dust or ice fog depending on the size of the crystals. At the Dome C station, numerous studies already focused on the diurnal and seasonal variations of the atmospheric boundary layer (e.g., Ricaud et al., 2012).

102   The objectives of the paper are mainly to investigate the processes that cause the presence

103 of thick cloud and diamond dust/ice fog episodes above the Dome C station based on

104 observations and verify whether operational models can estimate them. By combining

105 measurements from several instruments installed at the station, together with space-borne

106 measurements and model outputs, we intend to study the nature of the clouds and the

107 meteorological processes that favored their formation by using parameters such as tropospheric

108 temperature and absolute humidity, integrated water vapour, nebulosity, long- and shortwave

109 up- and downward radiations, together with the vertical distribution of aerosol depolarization

110 ratios.

111   We concentrate our efforts on two episodes: 15 March to 8 April 2011 and 4 to 5 March

112 2013. Several instruments have been used: 1) A ground-based microwave radiometer

113 (HAMSTRAD, H_2O Antarctica Microwave Stratospheric and Tropospheric Radiometers)

114 installed at Dome C that provided vertical profiles of tropospheric temperature and absolute

115 humidity with a 7-min integration time. 2) Daily radiosoundings launched at 12:00 UTC at

116 Dome C. 3) A tropospheric aerosol Lidar that provides aerosol depolarization ratio along the

117 vertical at Dome C. 4) Down- and upward short- and longwave radiations as obtained from

118 secondary standard pyranometers and pyrgeometer installed at Dome C and belonging to the

119 Baseline Surface Radiation Network (BSRN). 5) An ICE-CAMERA to detect at an hourly rate

120 the size of the ice crystal grains deposited at the surface of the camera. 6) Space-borne aerosol

121 depolarization ratio from the Cloud-Aerosol Lidar with Orthogonal Polarization (CALIOP)

122 Lidar aboard the CALIPSO platform along orbits close to the Dome C station. The time

123 evolution of the atmosphere over the 1-month period in 2011 has also been evaluated by

124 considering the outputs from the meso-scale model AROME (Seity et al., 2011) in 3

125 configurations. 1) "Operational", operating mode with a snow albedo of 0.80. 2) "Operational

126 with ice tuning", as in "Operational" but with a setting of snow albedo that can reach up to 0.85.

127 And finally 3) "ARPEGE micro-physics", as in "Operational with ice tuning" but includes the

128 physics of ARPEGE and a state-of-the-art scheme to represent the snow pattern taking into

129 account the roughness length. And finally, we will use the global-scale ARPEGE

130 meteorological analyses in 2013 selected over the Dome C station.

131 The manuscript is structured as follow. Section 2 presents all the data sets used in our study.

132 Section 3 investigates episode 1, namely the thick cloud and the diamond dust/ice fog episodes

133 during the 1-month period in 2011 considering the temporal evolution of the different

134 parameters above and in the surroundings of the Dome C station. Section 4 deals with episode

135 2 in 2013. The genesis of the thick cloud and the diamond dust/ice fog episodes is discussed in

136 Section 5. Finally, Section 6 concludes the study.

137

138 **2. Datasets**

139 **2.1. The HAMSTRAD Radiometer**

140 The HAMSTRAD (H_2O Antarctica Microwave Stratospheric and Tropospheric

141 Radiometers) instrument is a state-of-the-art microwave radiometer to probe the troposphere in

142 very cold and very dry environments in order to retrieve temperature and absolute humidity

143 vertical profiles, and IWV. Temperature profiles are obtained from the 51–59 GHz spectral

144 range, centered on the oxygen line. Absolute humidity profiles are retrieved from the 169–197

145 GHz spectral range, centred on the water vapour line. IWV is calculated from the water vapour

146 profile integrated along the vertical. Integration time is 7 min. The radiometer is presented in

147 Ricaud et al. (2010).

148 The instrument was sent to Dome C in January 2009. It has been running automatically

149 since January 2010. Science and validation studies using HAMSTRAD data are detailed in

150 Ricaud et al., 2012; 2013; 2014a-c; and 2015. All the HAMSTRAD data measured since 2009

151 are freely available at the following address:

152 http://www.cnrm.meteo.fr/spip.php?article961&lang=en. The radiometer sensitivity is very

153 high in the planetary boundary layer, high in the free troposphere and very weak in the upper

154 troposphere-lower stratosphere (Ricaud et al., 2015). The H_2O and temperature vertical

155 resolutions are ~20-50 m, ~100 m and ~500 m in the planetary boundary layer, in the free

156 troposphere and in the upper troposphere-lower stratosphere, respectively. Statistically, it has

157 been shown that, against radiosondes from 2009 to 2014, there is a 1-5 K cold bias below 4 km,

158 and a 5-10 K warm bias above, with a high time correlation (linear Pearson correlation

159 coefficient $r > 0.80$). There is a wet bias of 0.1-0.3 g m^{-3} below about 2 km and a dry bias of

160 ~0.1 g m^{-3} above, with a high time correlation below 4 km ($r > 0.70$). Yearly-averaged vertical

161 profiles of the biases in temperature and absolute humidity are also provided from 2009 to date

162 at the same http address. Note we have not debiased HAMSTRAD data in the present study.

163

2.2. Radiosondes

165 The programme of radiosoundings developed at Dome C is presented in Ricaud et al.

166 (2014a). Temperature and humidity biases against HAMSTRAD are shown in the previous

167 section. In the present study, the vertical profiles of temperature and humidity were taken from

168 RS92 radiosondes using the standard Vaisala evaluation routines without any correction of

169 sensor heating or time lag effect. We recall that the corrections performed on the radiosonde

170 data measured in 2009 according to Miloshevish et al. (2006) shown a weak impact (with a

171 maximum of +4% on IWV) on the vertical profiles (Ricaud et al., 2013). Furthermore,

172 considering the updated tools developed in Miloshevich et al. (2009), Tomasi et al. (2011 and

173 2012) found that, between 630 and 470 hPa, the correction factor for humidity estimated by the

174 radiosonde varied within 1.10-1.15 for daytime and within 0.98-1.00 for nighttime. It is

175 important to note that the 630-470 hPa layer is located between the ground and an altitude of

176 ~2 km which maximizes the calculation of IWV. A 1.2 K cold bias is also observed in the RS92

177 from the surface up to an altitude of ~4 km (Tomasi et al., 2011 and 2012).

178

179 **2.3. The Aerosol Lidar**

180 The aerosol lidar is an automatic backscatter and depolarization system in operation at

181 Dome C in relation with different scientific projects (http://lidarmax.altervista.org/lidar/

182 Antarctic LIDAR.php). Vertical profiles of aerosol and cloud structures are continuously

183 measured together with characterization of the physical phase of particles. Lidar data and false

184 color plots, obtained with an automated procedure, are delivered to Italy on a daily basis.

185 The Lidar system uses a Laser Quantel (Brio) at Dome C and operates at 532 nm to get

186 backscattering and depolarization ratio from 30 to 7000 m above ground with a 7.5-m vertical

187 resolution. The line of sight is zenith looking through a window enabling measurements in all-

188 weather conditions. The telescope has a 10-cm diameter, with 30-cm refractive optics and 0.15-

189 nm interference filter. It has already been used in several scientific studies, e.g. the radiative

190 properties of H_2O and clouds in the far infrared over Antarctica (Palchetti et al., 2015).

191

192 **2.4. CALIOP onboard CALIPSO**

193 The CALIPSO satellite has been launched to study the role clouds and aerosols play in the

194 Earth system that includes air quality, weather and climate. CALIPSO was launched on 28 April

195 2006 with the cloud profiling radar system on the CloudSat satellite. The CALIPSO satellite

196 comprises three instruments, the CALIOP Lidar, the Imaging Infrared Radiometer (IIR), and

197 the Wide Field Camera (WFC) (Winker et al., 2009).

198 CALIOP is a two-wavelength (532 nm and 1064 nm) polarization-sensitive lidar that

199 provides high-resolution vertical profiles of aerosols and clouds

200 (https://calipso.cnes.fr/en/CALIPSO/lidar.htm). CALIOP uses three receiver channels: one

measures the 1064 nm backscatter intensity and two channels measure orthogonally polarized components of the 532 nm backscattered signal. The receiver telescope is 1 metre in diameter. The full-angle field of view of the telescope is 130 µrad resulting in a footprint at the Earth's surface of about 90 metres. Algorithms have been developed to retrieve aerosols and cloud layers together with optical and microphysical properties (Young and Vaughan, 2009). Depolarization ratio estimated with version V3.01 is presented in our study.

2.5. The BSRN Network

The objective of the World Climate Research Programme (WCRP) Baseline Surface Radiation Network (BSRN) is to provide, using a high sampling rate, observations of the best possible quality, for short- and longwave surface radiation fluxes. These readings are taken from a small number of selected stations, including Dome C, in contrasting climatic zones, together with collocated surface and upper air meteorological data and other supporting observations. The incoming longwave and shortwave radiation components of the surface radiative balance were taken from the Dome C BSRN station, and measured with two Kipp & Zonen CM22 secondary standard pyranometers and two Kipp & Zonen CG4 Pyrgeometers, all operated according to BSRN guidelines (Lanconelli et al., 2011).

2.6. The ICE-CAMERA

At Dome C in 2013, an ICE-CAMERA was installed on the roof of the shelter where both the HAMSTRAD and the aerosol Lidar were set up. This camera was able to take on an hourly rate a picture of the ice crystal grains deposited at the surface of the camera. The ICE-CAMERA (http://lidarmax.altervista.org/englidar/_Antarctic%20Precipitation.php) is equivalent to a flatbed scanner. It was built in order to operate unattended in Polar Regions for the study of precipitating ice grains. Precipitation is collected on a glass plate, where it is photographed with

5 μm resolution hourly. After each scan, the glass plate is electrically-heated in order to sublimate the ice grains. Image-processing software is used for the automatic characterization and counting of grains.

2.7. The AROME Model

AROME is a small-scale numerical prediction model, operational at Meteo-France since December 2008. It was designed to improve short-range forecasts of severe events such as intense Mediterranean precipitations (Cévenole events), severe storms, fog, urban heat during heat waves. The physical parameterizations of the model come mostly from the MESO-NH model whereas the dynamic core is the ALADIN model. The size of the mesh is 2.5 km against 10 km for ARPEGE over France in 2014. The model is initialized from a 3D-var data assimilation system using radar reflectivity and Doppler wind. Five daily forecasts are made with AROME, thus helping to better predict meteorological events of the day and of the morrow (30 h forecast range). AROME was used within the GEWEX Atmospheric Boundary Layer Study 4 (GABLS4) to study the meteorological evolution over the Dome C station (Bazile et al., 2015).

For the study, three experiments at 2.5 km were used. Two based on the AROME configurations: 1) "Operational", operating mode with the default snow scheme (Douville et al., 1995) (labeled as 79HA). 2) "Operational with ice tuning", as in "Operational" but with a setting of a minimum snow albedo of 0.8 (labeled as 79YG). In the third one "ARPEGE microphysics", the AROME physics was replaced by the ARPEGE one used in the global model with the state-of-the-art scheme to represent the permanent snow with a minimum snow albedo of 0.8 valid over Dome C and a more accurate roughness length (labeled as 79Z6).

2.8. The ARPEGE Model

The ARPEGE model is the global model used for the numerical weather prediction (NWP) at Météo-France. In the present study, the operational configuration has been used with a stretched grid at high resolution over France (10 km) and a coarser grid over Australia of 60 km. At the South Pole, the horizontal resolution is about 50 km and the vertical grid has 70 levels with a first level at around 16 m above the ground. The assimilation tool is based on an incremental 4-dimensional variational (4D-Var) method. The physical package used in the ARPEGE model is at the state-of-the-art, with a Turbulent Kinetic Energy scheme associated with a mass flux scheme for the boundary layer (Bazile et al., 2011). The clouds and the micro-physics use 4 prognostic variables such as cloud water, cloud ice, rain and snow (Lopez, 2002; Bouteloup et al., 2005). The radiative transfer in the atmosphere is computed with the Rapid Radiative Transfer Model (RRTM) scheme (Mlawer et al., 1997) for the longwave and the shortwave with the Fouquart-Morcrette scheme (Fouquart and Bonnel, 1980; Morcrette et al., 2001).

3. Episode 1 on 15 March-8 April 2011

3.1. Clouds

In order to check whether clouds are present or not over the station during the two periods studied in detail, we consider the time evolution of the aerosol depolarization as measured by the Lidar installed at Dome C on 24-26 March and on 4-6 April 2011 (Fig. 1). On 24-26 March (Fig. 1 top), high depolarization ratios (greater than 30%), signature of ice particles, start increasing by the end of 24 March (22:00 UTC), reaching an altitude of 1.2-1.5 km, all over 25 March, and start decreasing on 26 March by 12:00 UTC. The vertical structures in the depolarization ratio fields are a signature of precipitation of ice particles (Mishchenko et al., 2000). On 26 March, at about 2 km altitude from 07:00 to 13:00 UTC, a layer of low

276   depolarization ratio (less than 14%) appears, that is a signature of liquid water cloud. In general,

277   over this period, the cloud is so opaque that the Lidar signal cannot penetrate the structure

278   beyond ~1.2 km altitude.

279   We gain more insight into the vertical structure of the cloud covering the Dome C station

280   by considering the space-borne CALIOP Lidar nighttime measurements performed on 25

281   March 2011 in the vicinity of the station. Figure 2 top left shows the Spaceborne Lidar CALIOP

282   measurements of depolarization ratio along one orbit in the vicinity of the Dome C station on

283   25 March 2011. We note that, at the location of the Dome C station (75°06'S, 123°21'E), the

284   depolarization ratio is greater than 0.4 (ice particles) from the ground (3233 m above mean sea

285   level, amsl) to about 10 km amsl, namely ~7 km above the ground. If we now combine the

286   downward and upward Lidar information, we can state that on 24-26 March 2011, a 7-km thick

287   ice cloud passed over the Dome C station and precipitated ice particles whilst, by the end of the

288   period, a low-altitude (~2 km) liquid water cloud was also present.

289   From Figure 1 bottom, high depolarization ratios (greater than 30%) from the Lidar

290   operating at Dome C start increasing by the middle of 4 April (12:00 UTC), reaching a

291   maximum altitude of 100 m, increasing up to 200 m on 5 April at 09:00 UTC, to finish

292   decreasing on 6 April by 12:00 UTC. The high depolarization ratio shows that the cloud is

293   constituted of ice crystals and, since there are no other layers higher in the troposphere, there is

294   little trace of precipitation. Considering the CALIOP space-borne Lidar measurements of

295   depolarization ratio (Fig. 2 top right) performed on 5 April 2011 in the vicinity of the Dome C

296   station, they also suggest a much thinner cloud from the ground to about 4 km amsl, namely

297   less than 1 km above the ground, with values ranging 0.1-0.2 (ice particles). Since there is little

298   precipitation and no presence of standard thick clouds above the station, the thin cloud episode

299   is traditionally attributed to a diamond dust/ice fog episode, rather frequent at the Dome C

300   station.

301   From Girard and Blanchet (2001), ice fog is distinguished from diamond dust by the high

302   concentration of ice crystal of smaller diameters. Ice fog, ice crystals are generally closer to

303   spherical shape and their number concentration exceeds 1000 L^{-1} while their mean diameter is

304   below 30 µm. From Walden et al. (2003), the atmospheric ice crystals over the Antarctic Plateau

305   in winter is mainly constituted of three major types: diamond dust, blowing snow and snow

306   grains. When sorted by number, Lawson et al. (2006) attribute 30% of the crystals recorded at

307   the South Pole Station to rosette shaped (mixed-habit rosettes, platelike polycrystals, and rosette

308   shapes with side planes), 45% to diamond dust (columns, thick plates, and plates), and 25% to

309   irregular. By mass, the percentages are 57% rosette shapes, 23% diamond dust, and 20%

310   irregular. In the literature of the ice crystals over Antarctica and particularly over the Antarctic

311   Plateau, there is little mention of ice fog except some studies performed in the coastal areas of

312   e.g. McMurdo in Lazzara (2010). Based on Gultepe et al. (2015) and Arctic studies, the

313   maximum size for ice fog crystals is about 200 µm with diamond dust ice crystal sizes greater

314   than 200 µm. In the Eastern Antarctic Plateau over all the seasons except summer, a strong

315   surface-based temperature inversion persists in which small ice crystals referred to as diamond

316   dust/ice fog form in the boundary layer (Walden et al., 2003). Classification of ice-cloud

317   particles is important to retrieve the shape of individual crystals and to estimate the radiative

318   impact of the clouds (Bailey and Hallett, 2009; Lindqvist et al., 2012). It is beyond the scope

319   of the present analysis to classify ice crystals measured over the Dome C station.

320   The time evolution of the nebulosity vs. height as calculated by AROME according to the

321   3 configurations over the period 25 March-8 April 2011 is displayed Figure 3. In two

322   configurations (operational and operational with ice tuning), clouds (traced by values of

323   nebulosity greater than 0.25) are calculated mainly over two single periods: 1) on 22 March

324   from 1 to 5 km, and 2) on 25-29 March from the ground to 6 km. Considering the third

325   configuration (ARPEGE microphysics), the period when clouds (traced by values of nebulosity

greater than 0.25) are present is much longer than the two first configurations since it almost covers the entire time interval under consideration. There are indeed the two periods previously cited, namely on 22 March, and 25-29 March, but they extend both in time (22-24 March and 25-30 March, respectively) and altitude (surface to 7 km). Other periods show some moderate values of nebulosity (0.10-0.25) on 15-17, 20 March, and 2, 3, 4, 6-7 April. These calculated clouds can be close to the ground or high in the free troposphere (4-6 km). In the three configurations, high nebulosity values (greater than 0.8) are calculated close to the surface (0-200 m). The AROME model tends to produce a sort of cloud residual in the planetary boundary layer in the three configurations analyzed.

3.2. Radiation

The time evolution of the downward and upward short- and longwave radiations as measured by the BSRN international network is displayed in Figure 4, together with the net irradiance (difference between the downward and the upward fluxes) from 15 March to 8 April 2011. The diurnal cycle of solar irradiance fluxes is clearly evidenced with the obvious maximum at local noon ranging between 350 W m^{-2} (at the beginning of the period) and 150 W m^{-2} (at the end of the period). Albedo over the whole period is found to range between 0.8 and 0.95 with daily minimum at local noon (not shown). The upward longwave radiation emitted by the surface is generally greater than the downward irradiance in clear sky conditions, while they became similar under overcast when thick cloudiness prevents radiative cooling. Consequently, alternating day and night periods in March and April, the net irradiance is negative except around local noon when it can be either positive or close to zero. But for the two periods considered so far, namely on 25-26 March and on 5 April, the radiation budget is significantly different from the average situation.

On 25 March, the longwave radiations (both downward and upward) are greater than the shortwave radiations (both downward and upward) even at local noon. The resulting effect is that the net irradiance is positive or close to zero over the whole period. This obviously indicates that a thick cloud is shielding the downward shortwave radiation (coming from the Sun) and increases the downward longwave radiation (coming from the cloud). Furthermore, there is a great probability a thick cloud is present over the Dome C station.

On 5 April, the situation is radically different. There was no abrupt increase of longwave downward radiation as on 25 March, so we can rule out the presence of a thick cloud above the station. Nevertheless, the situation is atypical since, at local noon, the downward shortwave radiation is only slightly greater than the upward shortwave radiation, and the net irradiance does not exhibit an obvious diurnal cycle maximizing at local noon. Consequently, even if the presence of a thick cloud has been ruled out from the longwave radiation analysis, both the shortwave and the total irradiance analyses tend to suggest the presence of a cloud, probably thin and/or close to the surface, in order to 1) slightly affect the downward longwave irradiance, and 2) strongly affect the diurnal cycle of the net irradiance. The next section investigates the evolution of temperature and water vapour over the same period.

3.3. Temperature and water vapour time evolutions

The time evolution of temperature and absolute humidity profiles as measured by HAMSTRAD from 0 to 5 km are shown Figures 5 and 6, respectively. In general, temperature and water vapour from HAMSTRAD show a maximum over the period 25-26 March (thick cloud episode) and a minimum over the period 5 April (diamond dust/ice fog episode). Along the vertical, these two episodes cover a wide domain from the ground to more than 3 km above the ground for temperature and up to 2.5-3 km above the ground for absolute humidity. The warm and wet period lasts 3-4 days and is associated with the thick cloud episode although the

cold and dry period is of a short duration, namely 1 day, and is associated with the diamond dust/ice fog episode. Note that the time evolution of temperature and water vapour over the 15 March-8 April 2011 as measured by HAMSTRAD is consistent with the one measured by the radiosondes and calculated by AROME (not shown).

4. Episode 2 on 4-5 March 2013

The second episode, which is much shorter than the first one, relies on the same datasets presented in Section 3. The only difference is that the model analyses are only from the meteorological operational model ARPEGE that routinely delivers since December 2011 every 6 hours (00:00, 06:00, 12:00, and 18:00 UTC) meteorological fields at the vicinity of the Dome C station.

4.1. Clouds

The depolarization ratio measured by the aerosol Lidar installed at Dome C from 4 to 5 March is shown on Figure 7. High depolarization ratios (greater than 30%) are present all over 4 March, reaching an altitude of 1.5-2.0 km, and start decreasing on 5 March by 00:00 UTC. The thick cloud shows vertical structures in the depolarization ratio fields that are a signature of precipitation of ice particles (see section 3.1). Between 13:00 and 14:00 UTC on 4 March and from 00:00 to 10:00 UTC on 5 March, depolarization ratios are much lower, reaching values of less than 10%. From 10:00 to 24:00 UTC on 5 March, depolarization ratios (Fig. 7) are very high (>40%), indicative of ice crystals, but confined from the surface to 100-200 m altitude indicative of the presence of diamond dust/ice fog. This is confirmed by the BSRN radiation measurements (see section 4.2).

We now can consider the time evolution of the number of ice crystals measured by the ICE-CAMERA integrated over one hour from 4 to 5 March 2013 above the Dome C station on

Figure 8. We notice that, from 00:00 to 10:00 UTC on 5 March, the number of ice crystals detected by the ICE-CAMERA dramatically decreased from ~700 to ~200, whatever the crystal ice habit size greater than 20 μm. There is also a strong Lidar raw signal (not shown) together with a low Lidar depolarization signal (Fig. 7) around 100 m, signature of liquid particles. Consequently, the reduced polarization detected in Fig. 7 reflects the presence of supercooled liquid water and not the presence of ice crystals. There are some traces of vertical structures present around 18:00 UTC, signature of precipitation, but very difficult to detect probably because the fall velocity of the ice crystals is much less than in the case of thick clouds. But it is beyond the scope of the present paper to discuss the fall velocity of the ice crystals.

Over this 2-day period, only one CALIOP/CALIPSO orbit has been analyzed in the vicinity of the Dome C station (Fig. 1 bottom) on 4 March (08:15 UTC) during the thick-cloud episode. On that day, the depolarization ratio is ranging 0.1-0.3 from the ground (3233 m amsl) to about 8 km amsl, namely ~5 km above the ground. Note that there is no CALIPSO orbit in the vicinity of the Dome C station in coincidence with the diamond dust/ice fog episode.

Now we consider the presence of clouds and/or ice/liquid particles over the 2-day period either from active and passive remote-sensing measurements or from ARPEGE analyses. The time evolution of ice water mixing ratio calculated by ARPEGE over Dome C is represented in the Figure 9 top together with the total precipitation flux over the 2-day period (Fig. 9 bottom). The ARPEGE simulation indicates an ice cloud from the surface to near 4 km above the ground on 4 March with the top altitude decreasing down to the surface on 5 March at 12:00 UTC. The main thick cloud calculated on 4 March is associated with ice precipitation from the altitude of ~3 km at 06:00 UTC down to ~2 km on 20:00 UTC (Fig. 9 bottom). This is in agreement with observations. Between 18:00 and 24:00 UTC on 5 March, there is also a trace of ice cloud from 0 to 1 km altitude. There is no longer trace of local precipitation after 03:00 UTC on 5 March. But this calculated ice cloud is much deeper than the one observed by the Lidar.

4.2. Radiation

The time evolution of the downward and upward short- and longwave radiations as measured by the BSRN international network is displayed in Figure 10, together with the net irradiance (difference between the downward and the upward fluxes) from 1 to 9 March 2013. As already presented in section 3.2, the diurnal cycle of solar irradiance fluxes mainly shows a clear-sky period over the Dome C station, except over the period from 4 March at 00:00 UTC to 6 March at 00:00 UTC. Indeed, on 4 March all day long, there is a net increase in the long-wave downward radiation from 80 to 120 W m^{-2} compared to the values from 1 to 3 March and from 7 to 9 March when we can expect the station is under clear sky conditions. Furthermore, from 12:00 to 24:00 UTC, the net irradiance is about –20 W m^{-2} on 4 March, whilst it is usually about –30 W m^{-2} in clear sky conditions. Consequently, there is a great probability a thick cloud is present over the Dome C station on 4 March during 24 h. On 5 March, between 12:00 and 24:00 UTC, the net irradiance is very low (about –50 W m^{-2}) compared to values of about –30 W m^{-2} in clear sky conditions. There is a slight increase of the longwave downward (90 W m^{-2}) and upward (140 W m^{-2}) fluxes on 5 March compared to the fluxes in clear sky conditions (70 and 120 W m^{-2}, respectively), but much less than fluxes in cloudy conditions (150 and 160 W m^{-2}, respectively). Consequently, this 12-hour period on 5 March can neither be attributed to clear sky nor to thick cloud episodes. Quantitatively, over the period 1-8 March 2013 (Figure 10), considering clear sky days (excluding 4 and 5 March), the net irradiance between 14:00 and 17:00 UTC is –30.55 W m^{-2} whilst on 4 March (thick cloud episode) the net irradiance has increased to –16.75 W m^{-2} and on 5 March (diamond dust/ice fog episode) the net irradiance has decreased to –45.52 W m^{-2}.

4.3. Temperature and water vapour evolutions

The temperature and the water vapour anomalies over the 2-day period are represented in the Figures 11 and 12, respectively as measured by HAMSTRAD and as calculated by ARPEGE.

Considering the 0-K temperature anomaly isoline (Fig. 11), both datasets show a warm period on 4 March (thick cloud episode) followed by a cold period on 5 March (diamond dust/ice fog episode) from the surface to about 2.4 km above the ground on 4 March by ARPEGE and to about 4.0 ± 0.5 km by HAMSTRAD. The 1.6-km difference between the altitude of the 0-K temperature anomaly isoline in HAMSTRAD and in ARPEGE data sets on 4 March might be due to the poor vertical resolution of HAMSTRAD compared to ARPEGE. Above this altitude, a cold period is followed by a warm period in the two datasets. Although the HAMSTRAD data are noisier than the ARPEGE data, the maxima and minima are consistently observed and calculated in the lowermost troposphere around 12:00-18:00 UTC on 4 March and around 18:00-22:00 UTC on 5 March, respectively. From the surface to about 4-5 km altitude, both data sets also show a wet period (Fig. 12) on 4 March (thick cloud episode) followed by a dry period (diamond dust/ice fog episode) on 5 March.

In general, in the lower troposphere, ARPEGE and HAMSTRAD temperature datasets are very consistent to each other (see Fig. 11). If we now consider into detail the evolution of the vertical temperature structures during the 2 episodes, using also radiosondes measurements at 12:00 UTC, interesting conclusions can be deduced from Figure 13. During the warm episode (thick cloud) on 4 March, there is a sharp positive vertical temperature gradient at 12:00 and 18:00 UTC within the first 100-200 m altitude layer in the planetary boundary layer from a very cold surface of about 230 K reaching a maximum of about 240-242 K. Above, the atmosphere is rather isothermal and starts cooling around 400-800 m. All the datasets are very consistent to each other. During the cold episode on 5 March, the lower troposphere is generally colder that

475 during the warm episode, but at 12:00 UTC there is no such a stable planetary boundary layer

476 as observed a day before since the vertical gradient is only of a 3 K over 500 m altitude instead

477 of 20 K over 200 m during the warm episode. Radiosonde, ARPEGE and HAMSTRAD profiles

478 are consistent to each other. At 18:00 UTC, in the core of the diamond dust/ice fog episode, the

479 vertical structure of the temperature observed by HAMSTRAD showing a positive gradient

480 (218 to 227 K from 100 to 500 m) is opposite to the negative gradient of ARPEGE temperature

481 (228 to 226 K from the surface to 400 m). Consistent with Figure 13, the radiative impact of

482 the thick cloud is to enlarge the net irradiance by about 15 W m^{-2} thus to locally increase

483 temperature as measured by HAMSTRAD and calculated by ARPEGE whilst the radiative

484 impact of the diamond dust/ice fog is to reduce the net irradiance by about 15 W m^{-2} thus to

485 locally decrease temperature as measured by HAMSTRAD but not calculated by ARPEGE.

486 Consequently, the ice cloud calculated by ARPEGE on 5 March over the vertical domain 0-1

487 km (Fig. 9) is certainly advected and cannot be considered as a diamond dust/ice fog episode

488 locally produced as suggested by the observations.

489 If we synthesize our findings, we can state the following. The time evolution of temperature,

490 absolute humidity, ice and aerosol fields obviously shows two episodes of abrupt changes.

491 Firstly, a warm and wet period is associated with a thick cloud that develops from the surface

492 to 5-8 km above the ground and is constituted of ice crystals that precipitate. Secondly, a cold

493 and dry period is associated with a thin cloud that develops close to the surface (100-200 m)

494 and is constituted of ice crystals with a longer suspension time in the air. This later episode is

495 known as diamond dust/ice fog episode. The operational models take into account interactions

496 between liquid and solid water phases but are enable to actually simulate the number of droplets

497 that depends on their sizes. Consequently, models can estimate the presence of thick clouds but

498 cannot reproduce diamond dust/ice fog episodes. A more sophisticated cloud microphysics such

499 as a two-moment scheme as LIMA (Liquid Ice Multiple Aerosols) scheme (Vié et al., 2016)

and an explicit aerosol scheme (Girard et al., 2001) would favour the local production of ice

crystals in the planetary boundary layer.

5. Discussions

In this section, we investigate the processes that contributed to the presence of a thick-cloud

and a diamond-dust/ice-fog episode above the Dome C station considering the origin of air

masses, the integrated water vapour fields over Antarctica and the temperature and water vapour

budgets calculated by ARPEGE.

5.1. Origin of Air Masses

Both the impact of the origin of air masses on the short-term variability of H_2O and

temperature and the high correlation coefficient (greater than 0.90) between water vapour and

temperature at Dome C over the entire year 2010 were presented in Ricaud et al. (2012 and

2014c) based on 5-day back-trajectory calculations. We propose, in the present study, to use

the same methodology to interpret the time evolution of the atmosphere during the two above-

mentioned episodes. We have thus considered a 5-day back trajectory study based upon the

European Centre for Medium-Range Weather Forecasts (ECMWF) analyses starting from the

Dome C location at five different pressure levels from the planetary boundary layer (650 and

600 hPa), to the free troposphere (500, 400 and 300 hPa).

For episode 1, Figure 14 (top left) shows the 5-day back-trajectories at the 5 selected pressure

levels during the warm and wet period (see the section 3) on 25 March 2011 at 12:00 UTC

corresponding to the time of maximum temperature and absolute humidity of an air parcel

issued from Dome C. In the lowermost layers (650 and 600 hPa), the air parcels are mainly

issued from the Antarctic continent. But higher up, at 500, 400 and 300 hPa, air masses are

coming from the oceanic middle latitudes, between Australia and New Zealand, imprint of

warm and wet air masses. When air masses in the free troposphere reach the Antarctic continent, they are uplifted and temperature decreases by more than 50 K (not shown). Note the air parcel at 400 hPa that is firstly originated from oceanic high latitudes in the vicinity of the Antarctic continent but moves towards the middle oceanic latitudes with a net subsidence and an increase of temperature of 30 K.

Regarding the diamond-dust/ice-fog period, Figure 14 (top right) shows the 5-day back-trajectories at the 5 selected pressure levels on 5 April 2011 at 12:00 UTC corresponding to the time of minimum temperature and absolute humidity of an air parcel issued from Dome C. We can note that all the calculated air masses are originated from the Antarctic plateau whatever the pressure level considered. Consequently, as already studied in Ricaud et al. (2012 and 2014c), we thus expect that both temperature and H_2O tends to decrease on 5 April at 12:00 UTC compared to the surrounding periods because air masses with continental origins produce a cold and dry atmosphere above Dome C (as on 5 April 2011).

For episode 2, Figure 14 bottom left shows the 5-day back-trajectories at the 4 selected pressure levels of 650, 600, 500 and 400 hPa during the warm and wet period (see section 4) on 4 March 2013 at 08:00 UTC corresponding to the time of maximum temperature and absolute humidity of an air parcel issued from Dome C. At 650 hPa, the air parcel has a continental origin but migrates very close to the coast 2 days before reaching Dome C. Above, at 600, 500 and 400 hPa, all the air masses are coming from the oceanic middle-high latitudes ranging from 47°S to 63°S and from the surface to ~680 hPa, namely imprint of warm and wet air masses. As for episode 1, when air parcels in the free troposphere reach the Antarctic continent, they are uplifted and temperature decreases by 20-30 K (not shown). On 5 March at 18:00 UTC (Fig. 14 bottom right) during the cold and dry period of episode 2 corresponding to the time of minimum temperature and absolute humidity, the meteorological situation is radically different. Whatever the pressure level considered, the air parcels are all confined to

550   the Antarctic plateau in the vicinity of the Dome C station, explaining again, as for episode 1,

551   the cold and dry atmosphere observed during episode 2.

552

553   **5.2. Integrated Water Vapour over Antarctica**

554   The Integrated Water Vapour (IWV) fields calculated by the NCEP/NCAR operational

555   analyses (Kalnay et al., 1996) on 25 March 2011 and 5 April 2011 for episode 1 over the

556   Antarctic continent (Figure 15 top left and right, respectively) show that the Eastern Antarctic

557   plateau is much wetter on 25 March than on 5 April. The IWV calculated over the Dome C

558   station is ~1.4 kg m^{-2} on 25 March 2011 and ~0.6 kg m^{-2} on 5 April 2011 in excellent agreement

559   with the HAMSTRAD measurements (see section 3.3). This is induced by the oceanic-origin

560   flux bringing warm and wet air masses over the Dome C station on 25 March and by the

561   continent-origin flux bringing cold and dry air masses over the station on 5 April. The same

562   exercise can be performed for the episode 2 (Figure 15 bottom left and right, respectively)

563   considering the IWV fields as calculated by the NCEP/NCAR operational analyses on 4 and 5

564   March 2013. There, the IWV fields above Dome C show a similar pattern between 4 and 5

565   March but with a smaller wet inflection on 4 March compared to 5 March with daily averaged

566   values of ~0.6 and ~0.4 kg m^{-2}, respectively consistent with the daily-averaged values obtained

567   at Dome C with HAMSTRAD (~0.55 and ~0.30 kg m^{-2}, respectively). Consequently,

568   considering episodes 1 and 2, the thick-cloud episodes observed during the warm and wet

569   period above Dome C are attributed to air masses with an oceanic origin whilst the diamond

570   dust/ice fog episodes occurred during the cold and dry period are attributed to air masses with

571   continental origins.

572

573

574

5.3. Temperature and Water Vapour Budgets

Here, we attribute the tendencies of temperature calculated by ARPEGE during episode 2 among radiation, turbulence, microphysics, and total advection and the tendencies of water vapour among turbulence, microphysics, and total advection. Figure 16 shows the temperature budget calculated on 4 March 2013 over the warm and wet 12-h period 00:00-12:00 UTC and on 5 March 2013 over the dry and cold 12-h period 06:00-18:00 UTC whilst Figure 17 focuses on the water vapour budget.

For altitudes greater than ~100 m (3333 m amsl) above the ground on 4 March and greater than ~200 m on 5 March, the temperature tendency of the warm (Fig. 16 left) and of the cold (Fig. 16 right) periods is mainly dominated by the advection processes (red lines). This is fully consistent with the interpretation of the origin of air masses (previous subsection). Nevertheless, in the planetary boundary layer below approximately 100 m on 4 March and below 200 m on 5 March, the temperature tendency of the two periods is also governed by the vertical mixing done by the turbulent processes (green line). Indeed, turbulence always tends to stabilize the atmosphere impacted by radiative or dynamical forcing. The effect of the radiative cooling on the surface temperature and its impact on the boundary layer is clearly shown on 5 March (Fig. 16 right).

As for temperature, the water vapour tendency of the two periods also needs to be separated at ~100 and ~200 m above the ground on 4 and 5 March, respectively. Above these two limits, the water vapour tendency of the warm period (Fig. 17 left) and of the cold (Fig. 17 right) periods is governed by both the advection and the microphysical processes. On 4 March, warmer and more humid air is advected (total water vapour tendency in Fig. 17 left and total temperature advection in Fig. 16 left are positive), so the microphysics tend to create some clouds by condensation (negative microphysics tendency, blue line on Fig. 17 left) with weak precipitations close to the surface (~18 mm in 12 hours, not shown). On 5 March (Fig. 17 right),

the water vapour advection (red line) is negative so a drier air is advected toward the Dome C station. Below ~200 m, advection, turbulence and microphysical (precipitation) processes compete to dehydrate the planetary boundary layer.

In general, this reinforces our conclusions of thick cloud episodes driven by warm and wet air masses of oceanic origin and of diamond dust/ice fog episodes driven by cold and dry air masses of continental origin. Nevertheless, in the planetary boundary layer below approximately ~100-200 m, the water vapour tendency of the two periods is competing between advection, microphysical and turbulence processes.

6. Conclusions

The present study takes the opportunity of combining several measurements and operational model outputs to study the short-term evolution of the Antarctic atmosphere above the Dome C station focusing on episodes of thick cloud and diamond dust/ice fog. The objectives of the paper are mainly to investigate the processes that cause these episodes based on observations and to verify whether operational models can evaluate them. From 15 March to 8 April 2011 and from 4 to 5 March 2013, the atmosphere has been probed by several instruments. 1) A ground-based microwave radiometer (HAMSTRAD) installed at Dome C that provided vertical profiles of tropospheric temperature and absolute humidity with a 7-min integration time. 2) Daily radiosoundings launched at 12:00 UTC at Dome C. 3) A tropospheric aerosol Lidar that provides aerosol depolarization ratio along the vertical. 4) Down- and upward short- and longwave radiations from an instrument installed at Dome C belonging to the BSRN network. 5) An ICE-CAMERA to detect at an hourly rate the size of the ice crystal grains deposited at the surface of the camera. 6) Space-borne aerosol depolarization ratio from the CALIOP Lidar aboard the CALIPSO platform along orbits close to the Dome C station.

624   The time evolution of the atmosphere over the 1-month period in 2011 has also been

625   evaluated by considering the outputs from the mesoscale model AROME in 3 configurations.

626   1) "Operational", operating mode with a snow albedo of 0.80. 2) "Operational with ice tuning",

627   as in "Operational" but with a setting of snow albedo that can reach up to 0.85. And finally 3)

628   "ARPEGE micro-physics", as in "Operational with ice tuning" but includes the physics of

629   ARPEGE and a state-of-the-art scheme to represent the snow pattern taking into account the

630   roughness length. The ARPEGE global-scale meteorological model analyses gave the state of

631   the atmosphere and relevant prognostics (ice precipitation, temperature and water vapour

632   budget) on 4 and 5 March 2013.

633   Considering upward and downward active measurements of aerosols from two Lidars

634   installed at Dome C and aboard a spaceborne platform, respectively, together with downward

635   and upward longwave radiations, the signature of a thick cloud with high depolarization ratios

636   (greater than 30%) is detected during 2 periods (24-26 March 2011 and 4 March 2013) from

637   the surface to ~5-7 km above the ground with precipitation of ice particles and the presence of

638   a supercooled liquid water cloud with low depolarization ratios (~10%). These 2 periods are

639   shown to be warm and wet by considering HAMSTRAD and radiosonde measurements. Over

640   2 other periods (5 April 2011 and 5 March 2013), diamond dust and/or ice fog are detected with

641   high depolarization ratios (greater than 30%) in the planetary boundary layer to a maximum

642   altitude of 100-300 m above the ground with little trace of precipitation. These 2 periods are

643   shown to be cold and dry by considering HAMSTRAD and radiosonde measurements.

644   The presence of a thick cloud during the warm and wet periods of 2011 and 2013 is

645   calculated by the operational models of AROME and ARPEGE in the free troposphere

646   extending from the surface to ~6 km above the ground. In the three configurations of AROME,

647   high nebulosity values (greater than 0.8) are calculated close to the surface (0-200 m), almost

648   systematically in the two first configurations (operational and operational with ice tuning). The

649 AROME model tends to produce a sort of cloud residual in the planetary boundary layer in the

650 three configurations analyzed so the presence of a thin cloud close to the surface cannot be

651 ruled out. ARPEGE also calculates ice precipitation during the thick cloud event. But the

652 diamond dust/ice fog episodes have not been evaluated in the planetary boundary layer during

653 the cold and dry periods by the operational models. No liquid water clouds have been estimated

654 by the ARPEGE analyses. Although operational models can reproduce thick cloud episodes in

655 the free troposphere, they cannot evaluate the diamond dust/ice fog episodes in the planetary

656 boundary layer because they require to use more sophisticated cloud and aerosol microphysics

657 schemes.

658   Considering 5-day back trajectories from Dome C and global distributions of IWV over the

659 Antarctic in 2011 and 2013 tends to show that the thick-cloud episodes observed during the

660 warm and wet periods above Dome C can be attributed to air masses with an oceanic origin

661 whilst the diamond dust/ice fog episode occurring during the cold and dry periods can be

662 attributed to air masses with continental origins. Thus, diamond dust/ice fog episodes are driven

663 by local processes whilst thick cloud episodes are driven by regional processes. This is

664 confirmed by the ARPEGE temperature tendencies calculated during the warm and the cold

665 periods of 2013 that are mainly dominated by the advection components whilst the water vapour

666 tendencies are governed by both the advection and the microphysical processes.

667

668 **Acknowledgment**

669   The present research project HAMSTRAD programme (910) has been performed at the

670 Dome C station and was supported by the French Polar Intitute, Institut polaire français Paul-

671 Emile Victor (IPEV), the Institut National des Sciences de l'Univers (INSU)/Centre National

672 de la Recherche Scientifique (CNRS), Météo-France and the Centre National d'Etudes

673 Spatiales (CNES). The permanently manned Concordia station is jointly operated by IPEV and

674 the Italian Programma Nazionale Ricerche in Antartide (PNRA). We would like to thank all the

675 winterover personels who worked at Dome C on the different projects: HAMSTRAD, Routine

676 Meteorological Observations (RMO), aerosol Lidar and BSRN. Thanks to the British

677 Atmospheric Data Centre, which is part of the Natural Environment Research Council (NERC)

678 National Centre for Atmospheric Science (NCAS), for the calculation of trajectories and access

679 to European Centre for Medium-Range Weather Forecasts (ECMWF) data. We have used

680 NCEP Reanalysis data provided by the NOAA/OAR/ESRL PSD, Boulder, Colorado, USA,

681 from their Web site at http://www.esrl.noaa.gov/psd/. The authors also would like to thank the

682 CALIPSO science team for providing the CALIOP images at http://www-

683 calipso.larc.nasa.gov/. HAMSTRAD data are available at

684 http://www.cnrm.meteo.fr/spip.php?article961&lang=en. RMO data are available at

685 http://www.climantartide.it. We finally would like to thank the two anonymous reviewers to

686 their fruitful comments.

687

688

689 **References**

690 Adhikari, L., Wang, Z. and Deng, M.: Seasonal variations of Antarctic clouds observed by

691 CloudSat and CALIPSO satellites, J. Geophys. Res., 117, D04202,

692 doi:10.1029/2011JD016719, 2012.

693 Argentini, S., Viola, A., Sempreviva, A. M. and Petenko, I.: Summer boundary-layer height at

694 the plateau site of Dome C, Antarctica, Bound.-Layer Meteor., 115, 409-422, 2005.

695 Bailey, M. P., and Hallett, J: A comprehensive habit diagram for atmospheric ice crystals:

696 Confirmation from the laboratory, AIRS II, and other field studies, J. Atmos. Sci., 66, 2888-

697 2899, 2009.

698 Bazile, E., Marquet, P., Bouteloup, Y., and Bouyssel, F.: The Turbulent Kinetic Energy (TKE)

699 scheme in the NWP models at Météo-France, ECMWF Proceedings "Workshop on Diurnal

700 cycles and the stable boundary layer", 127-136, 2011.

701 Bazile, E., Couvreux, F., Le Moigne, P., and Genthon, C.: First Workshop on the GABLS-4

702 Intercomparison, GEWEX Newsletter, pp18-19, August 2015.

703 Bouteloup, Y., Bouyssel, F., and Marquet, P.: Improvements of Lopez's progonostic large scale

704 cloud and precipitation scheme, ALADIN Newsletter, 28, 66-73, 2005.

705 Brasseur, G. P., Orlando, J. J., and Tyndall, G. S.: Atmospheric chemistry and global change,

706 2nd edition, Oxford University Press, New York, Oxford, ISBN-0-19-510521-4, 1999.

707 Davis, D., Nowak J. B., Chen G., Buhr M., Arimoto R., Hogan A., Eisele F., Mauldin L., Tanner

708 D., Shetter R., Lefer B., and McMurry P.: Unexpected high levels of NO observed at South

709 Pole, Geophys. Res. Lett., 28, 3625-3628, 2001.

710 Douville, H., Royer, J.-F. and Mahfouf, J.-F.: A new snow parameterization for the Météo-

711 France climate model, Part I : Validation in stand-alone experiments, Clim. Dynam., 12,

712 21-35, 1995.

713   Dufresne, J. L. and Bony, S.: An assessment of the primary sources of spread of global warming

714   estimates from coupled atmosphere-ocean models, J. Climate, 21, 5135-5144, 2008.

715   Fouquart, Y., and Bonnel, B.: Computations of solar heating of the earth's atmosphere: a new

716   parameterization, Beitr. Phys. Atmosph., 53, 35-62, 1980.

717   Girard, E. and Blanchet, J. P.: Microphysical parameterization of Arctic diamond dust, ice fog,

718   and thin stratus for climate models. J. Atmos. Sci., 58, 1181-1198, 2001.

719   Gultepe, I., Kuhn, T., Pavolonis, M., Calvert, C., Gurka, J., Heymsfield, A. J., Liu, P. S. K.,

720   Zhou, B., Ware, R., Ferrier, B., Milbrandt, J. and Berstein, B.:Ice fog in Arctic during

721   FRAM-ICE Fog project: Aviation and Nowcasting Applications, Bull. Am. Meteor. Soc.,

722   95, 211-226, 2014.

723   Hines, K. M., Bromwich, D. H., Rasch, P. J. and Iacono, M. J.: Antarctic clouds and radiation

724   within the NCAR climate models, J. Climate, 17, 1198–1212, doi:10.1175/1520-

725   0442(2004)017, 2004.

726   Hudson, S. R., Warren, S. G., Brandt, R. E., Grenfell, T. C., and Six, D.: Spectral bidirectional

727   reflectance of Antarctic snow: Measurements and parameterization, J. Geophys. Res., 111,

728   D18106, doi:10.1029/2006JD007290, 2006.

729   Kalnay, E., Kanamitsu, M., Kistler, R., Collins, W., Deaven, D., Gandin, L., Iredell, M., Saha,

730   S., White, G., Woollen, J., Zhu, Y., Leetmaa, A., Reynolds, R., Chelliah, M., Ebisuzaki,

731   W., Higgins, W. Janowiak, J., Mo, K. C., Ropelewski, C., Wang, J., Jenne, R. and Dennis

732   Joseph, D.: The NCEP/NCAR 40-Year Reanalysis Project, Bull. Amer. Meteor. Soc., 77,

733   437–471, 1996.

734   Lanconelli, C., Busetto, M., Dutton, E. G., König-Langlo, G., Maturilli, M., Sieger, R., Vitale,

735   V. and Yamanouchi, T.: Polar baseline surface radiation measurements during the

736   International Polar Year 2007-2009: Earth System Science Data, 3(1), 1-8,

737   doi:10.5194/essd-3-1-2011, 2011.

738   Lawson, R. P., Baker, B. A., Zmarzly, P., O'Connor, D., Mo, Q., Gayet, J. F. and Shcherbakov,

739   V.: Microphysical and optical properties of atmospheric ice crystals at South Pole Station,

740   J. Appl. Meteor., 45, 1505-1524, 2006.

741   Lazzara, M.: Diagnosing Antarctic fog, 5th International Conference on Fog, Fog Collection

742   and Dew, Münster, Germany, 25-30 July 2010. Vol. 1, p. 150.

743   (http://meetingorganizer.copernicus.org/FOGDEW2010/FOGDEW2010-150.pdf)

744   Lindqvist, H., Muinonen, K., Nousiainen, T., Um, J., McFarquhar, G. M., Haapanala, P.,

745   Makkonen, R. and Hakkarainen, H.: Ice-cloud particle habit classification using principal

746   components, J. Geophys. Res., 117, D16206, doi:10.1029/2012JD017573, 2012.

747   Lopez, P.: Implementation and validation of a new prognostic large-scale cloud and

748   precipitation scheme for climate and data assimilation purposes, Q. J. R. Meteorol. Soc.,

749   128, 229-257, 2002.

750   Lubin, D., Chen, B., Bromwich, D. H., Somerville, R. C., Lee, W. H., and Hines, K. M.: The

751   Impact of Antarctic Cloud Radiative Properties on a GCM Climate Simulation, J. Climate,

752   11, 447-462, 1998.

753   Miloshevich, L. M., Vömel, H., Whiteman, D. N., Lesht, B. M., Schmidlin, F. J. and Russo, F.:

754   Absolute accuracy of water vapor measurements from six operational radiosonde types

755   launched during AWEX-G and implications for AIRS validation, J. Geophys. Res., 111,

756   D09S10, doi:10.1029/2005JD006083, 2006.

757   Miloshevich, L. M., Vömel, H., Whiteman, D. N. and Leblanc, T.: Accuracy assessment and

758   corrections of Vaisala RS92 radiosonde water vapour measurements, J. Geophys. Res., 114,

759   D11305, doi:10.1029/2008JD011565, 2009.

760   Mishchenko, M. I., J. W. Hovenier, and L. D. Travis (Eds.): Light Scattering by Nonspherical

761   Particles: Theory, Measurements, and Applications. Academic Press. Chapter 14, 393-416,

762   2000.

763   Mlawer, E. J., Taubman, S. J., Brown, P. D., Iacono, M. J. and Clough, S. A.: Radiative transfer

764   for inhomogeneous atmospheres: RRTM, a validated correlated-k model for the longwave,

765   J. Geophys. Res., 102D, 16663-16682, 1997.

766   Morcrette, J.-J., Mlawer, E. J., Iacono, M. J. and Clough, S. A.: Impact of the radiation transfer

767   scheme RRTM in the ECMWF forecasting system, ECMWF Newsletter, 91, 2-9, 2001.

768   Palchetti, L., Bianchini, G., Di Natale, G., and Del Guasta, M.: Far infrared radiative properties

769   of water vapor and clouds in Antarctica, B. Am. Meteorol. Soc., 96, 1505-1518,

770   doi:10.1175/BAMS-D-13-00286.1, 2015

771   Pirazzini, R.: Surface albedo measurements over Antarctic sites in summer, J. Geophys. Res.,

772   109, D20118, doi:10.1029/2004JD004617, 2004.

773   Ricaud, P., Gabard, B., Derrien, S., Chaboureau, J.-P., Rose, T., Mombauer, A. and Czekala,

774   H.: HAMSTRAD-Tropo, A 183-GHz Radiometer Dedicated to Sound Tropospheric Water

775   Vapor Over Concordia Station, Antarctica, IEEE Trans Geosci Remote Sens., 48, 1365–

776   1380, doi: 10.1109/TGRS.2009.2029345, 2010.

777   Ricaud, P., Genthon, C., Durand, P., Attié, J.-L., Carminati, F., Canut, G., Vanacker, J.-F.,

778   Moggio, L., Courcoux, Y., Pellegrini, A. and Rose, T.: Summer to Winter Diurnal

779   Variabilities of Temperature and Water Vapor in the lowermost troposphere as observed by

780   the HAMSTRAD Radiometer over Dome C, Antarctica, Bound.-Layer Meteor., 143, 227–

781   259, doi:10.1007/s10546-011-9673-6, 2012.

782   Ricaud, P., Carminati, F., Attié, J.-L., Courcoux, Y., Rose, T., Genthon, C., Pellegrini, A.,

783   Tremblin, P. and August, T: Quality Assessment of the First Measurements of Tropospheric

784   Water Vapor and Temperature by the HAMSTRAD Radiometer over Concordia Station,

785   Antarctica, IEEE Trans Geosci Remote Sens., 51, 3217–3239, doi:

786   10.1109/TGRS.2012.2225627, 2013.

787 Ricaud, P., Carminati, F., Courcoux, Y., Pellegrini, A., Attié, J.-L., El Amraoui, L., Abida, R.,

788   Genthon, C., August, T. and Warner, J.: Statistical Analyses and Correlation between

789   Tropospheric Temperature and Humidity at Dome C, Antarctica, Antarct. Sci., 26, 290 –

790   308. doi:10.1017/S0954102013000564, 2014a.

791 Ricaud, P.: Variabilités de la vapeur d'eau et de la température troposphérique au Dôme C

792   (station Concordia), Antarctique. Partie I : l'instrument Hamstrad, La Météorologie, 84,

793   15-28, doi:10.4267/2042/53184, 2014b.

794 Ricaud, P.: Variabilités de la vapeur d'eau et de la température troposphérique mesurées par le

795   radiomètre micro-onde HAMSTRAD au Dôme C, Antarctique. Partie II : Résultats

796   scientifiques, La Météorologie, 85, 35-46, doi:10.4267/2042/53749, 2014c.

797 Ricaud, P., Grigioni, P., Zbinden, R., Attié, J.-L., Genoni, L., Galeandro, A., Moggio, A.,

798   Montaguti, S., Petenko, I. and Legovini, P.: Review of tropospheric temperature, absolute

799   humidity and integrated water vapour from the HAMSTRAD radiometer installed at Dome

800   C, Antarctica, 2009–14, Antarct. Sci., 27, 598-616, doi:10.1017/S0954102015000334,

801   2015.

802 Seity, Y., Brousseau, P., Malardel, S., Hello, G., Bénard, P., Bouttier, F., Lac, C. and Masson,

803   V.: The AROME-France Convective-Scale Operational Model, Mon. Wea. Rev., 139, 976–

804   991, 2011.

805 Tomasi, C., B. Petkov, E. Benedetti, V. Vitale, A. Pellegrini, G. Dargaud, L. De Silvestri, P.

806   Grigioni, E. Fossat, W.L. Roth, and L. Valenziano: Characterization of the atmospheric

807   temperature and moisture conditions above Dome C (Antarctica) during austral summer

808   and fall months, J. Geophys. Res., lll, D20305, doi:10.1029/2005jD006976, 2006.

809 Tomasi, C., Petkov, B., Benedetti, E., Valenziano, L. and Vitale, V.: Analysis of a 4 year

810   radiosonde dataset at Dome C for characterizing temperature and moisture conditions of the

811   Antarctic atmosphere, J. Geophys. Res., 116, D15304, doi:10.1029/2011JD015803, 2011.

812   Tomasi, C., Petkov, B. H. and Benedetti, E.: Annual cycles of pressure, temperature, absolute

813   humidity and precipitable water from the radiosoundings performed at Dome C, Antarctica,

814   over the 2005-2009 period, Antarct. Sci., 24, 637–658, doi:10.1017/S0954102012000405,

815   2012.

816   Tremblin, P., V. Minier, N. Schneider, G. Al. Durand, M. C. B. Ashley, J. S. Lawrence, D. M.

817   Luong-van, J. W. V. Storey, G. An. Durand, Y. Reinert, C. Veyssiere, C. Walter, P. Ade,

818   P. G. Calisse, Z. Challita, E. Fossat, L. Sabbatini, A. Pellegrini, P. Ricaud and J. Urban:

819   Site testing for submillimetre astronomy at Dome C in Antarctica, Astronomy and

820   Astrophysics, 535 A112, DOI: http://dx.doi.org/10.1051/0004-6361/201117345, 2011.

821   Turner, J., Lachlan-Cope, T. A., Colwell, S., Marshall, G. J. and Connolley, W. M.: Significant

822   Warming of the Antarctic Winter Troposphere, Science, 311, doi:10.1126/science.1121652,

823   2006.

824   Vié, B., Pinty, J. P., Berthet, S., & Leriche, M. : LIMA (v1. 0): A quasi two-moment

825   microphysical scheme driven by a multimodal population of cloud condensation and ice

826   freezing nuclei. Geosci. Model Dev., 9, 567-586, 2016.

827   Walden, V. P., Warren, S. G. and Tuttle, E.: Atmospheric ice crystals over the Antarctic Plateau

828   in winter, J. Appl. Meteorol., 42, 1391-1405, 2003.

829   Winker, D. M., Vaughan, M. A., Omar, A., Hu, Y., Powell, K. A., Liu, Z., Hunt, W. H. and

830   Young, S. A.: Overview of the CALIPSO mission and CALIOP data processing algorithms,

831   J. Atmos. Oceanic Technol., 26, 2310-2323, 2009.

832   Young, S. A. and Vaughan, M. A.: The retrieval of profiles of particulate extinction from Cloud

833   Aerosol Lidar Infrared Pathfinder Satellite Observations (CALIPSO) lidar data: Algorithm

834   description, J. Atmos. Oceanic Technol., 26, 1105–1119, 2009.

835

Figure Caption
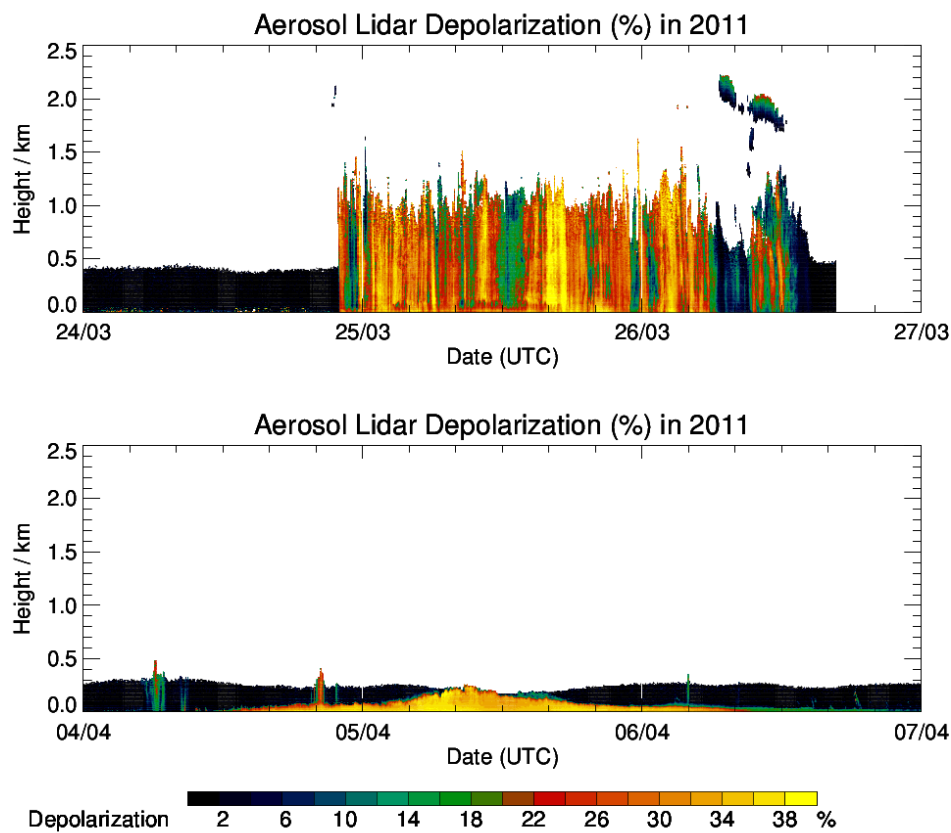
Fig. 1: (Top, from left to right) Aerosol depolarization as measured by the Lidar installed at the Dome C station over the period 24-26 March 2011. (Bottom, from left to right) Aerosol depolarization as measured by the Lidar installed at the Dome C station over the period 4-6 April 2011.

843

844
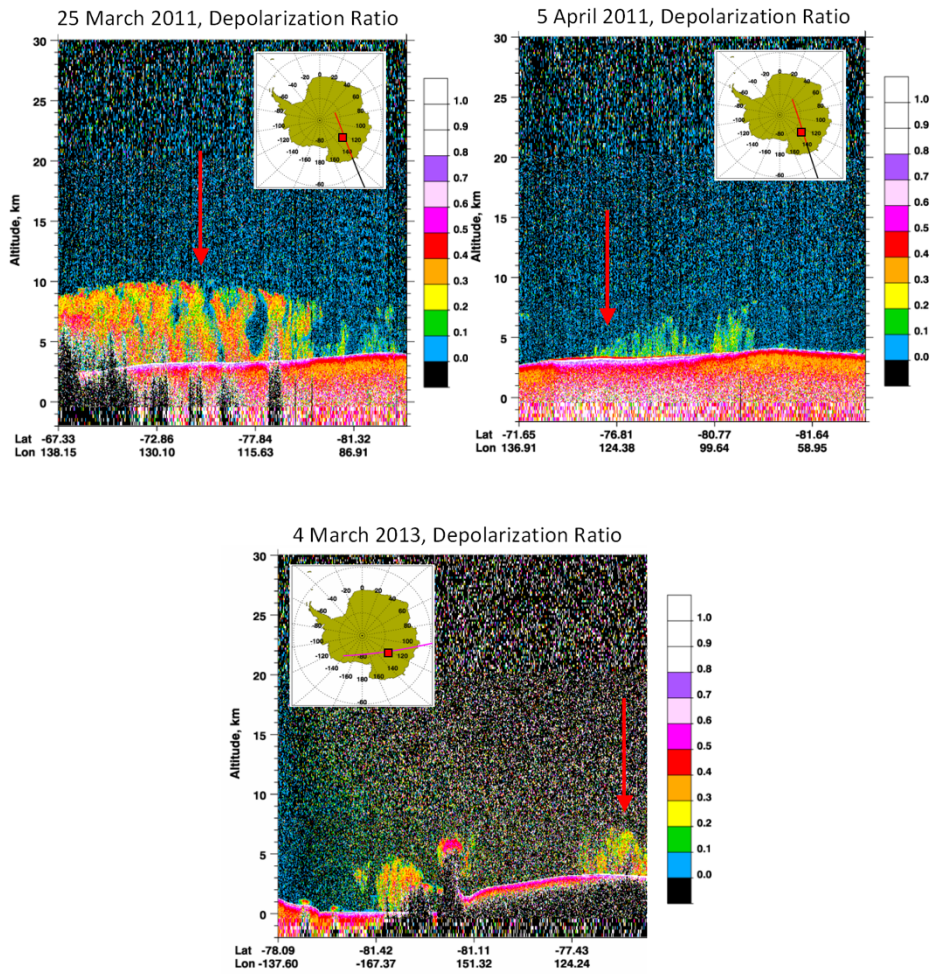
845 **Fig. 2:** Spaceborne Lidar CALIOP measurements of depolarization ratio along one orbit in the

846 vicinity of the Dome C station on 25 March 2011 (top left), 5 April 2011 (top right) and 4

847 March 2013 (bottom). The red square represents the location of the Dome C station. The red

848 vertical arrow represents the approximate location of the Dome C station.

849

850
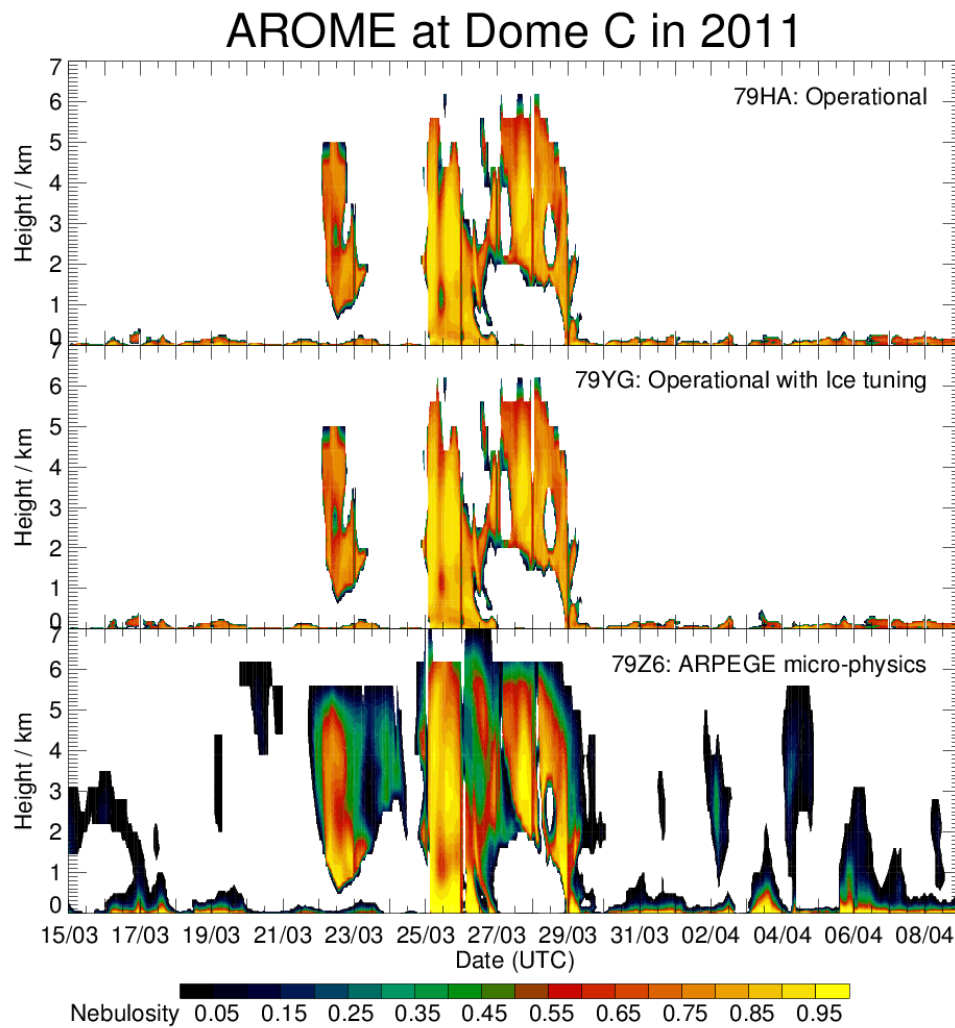
851
852
853 **Fig. 3:** (From top to bottom) Time evolution of nebulosity from 15 March to 8 April 2011 above

854 Dome C as calculated by the mesoscale model AROME according to different runs: operational

855 (top), operational with ice tuning (center) and considering ARPEGE micro-physics (bottom).

856 See the text for further information regarding the AROME runs.

857

858
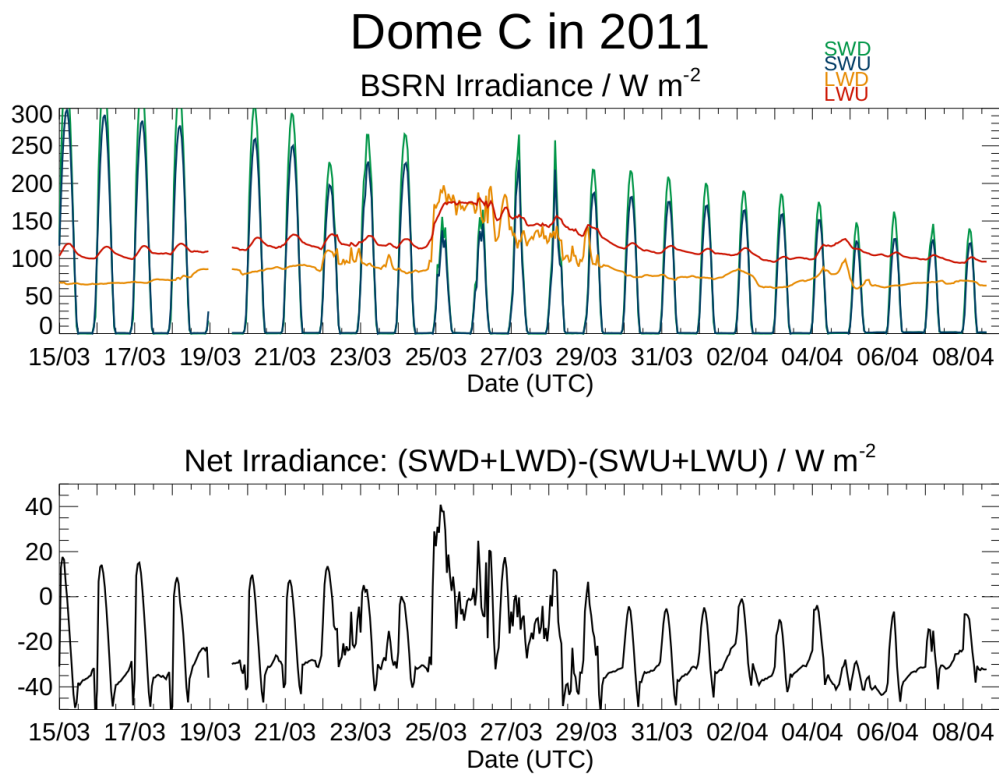
859 **Fig. 4:** (Top) Time evolution of downward shortwave radiation (SWD, green line), upward

860 shortwave radiation (SWU, blue line), downward longwave radiation (LWD, orange line), and

861 upward longwave radiation (LWU, red line) from 15 March to 8 April 2011 above Dome C as

862 measured by the BSRN instruments. (Bottom) Net irradiance (SWD+LWD-SWU-LWU) as

863 measured by the BSRN instruments.

864

865

866
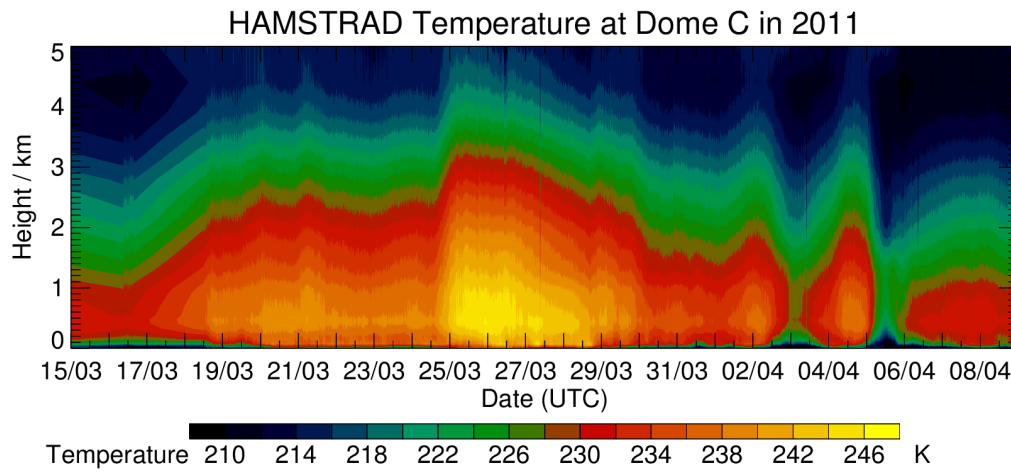
867 **Fig. 5:** Time evolution of temperature from 15 March to 8 April 2011 above Dome C as

868 measured by the HAMSTRAD radiometer from 0 to 5 km.

869

870

871
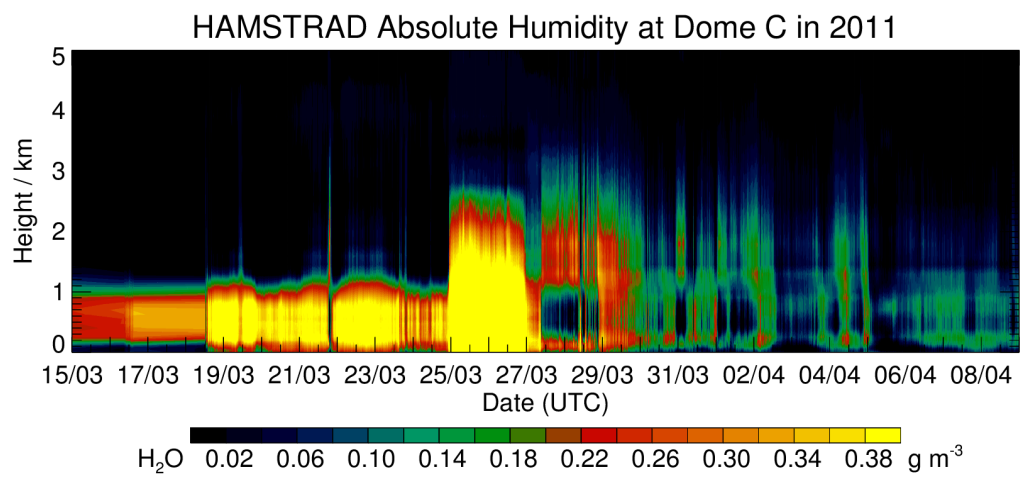
872

873 **Fig. 6:** Time evolution of absolute humidity from 15 March to 8 April 2011 above Dome C as

874 measured by the HAMSTRAD radiometer from 0 to 5 km.

875

876

877
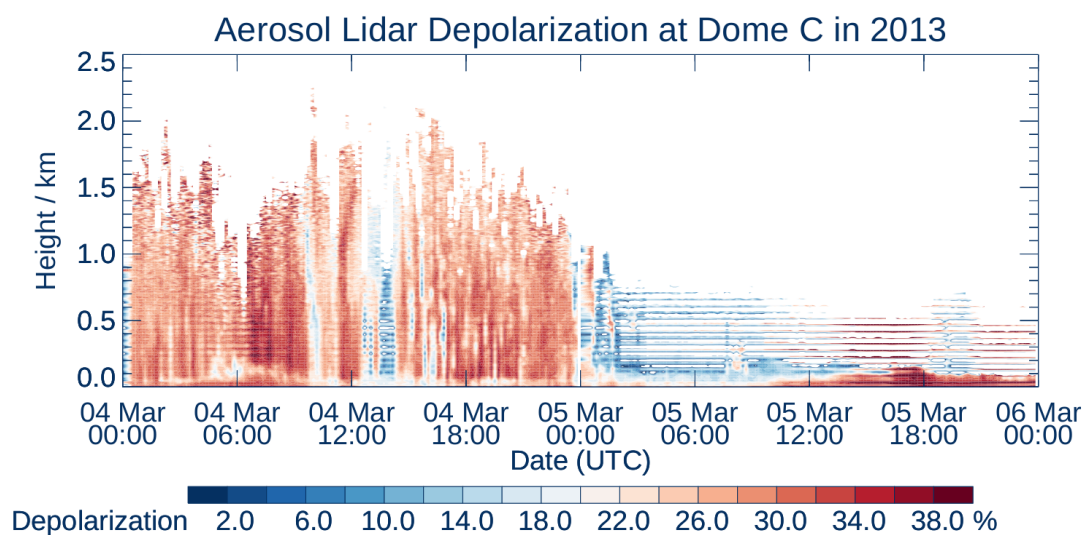
878   **Fig. 7:** Time evolution of the Depolarization ratio (%) from 4 to 5 March 2013 above the Dome

879   C station as measured by the aerosol Lidar installed at Dome C.

880

881

882
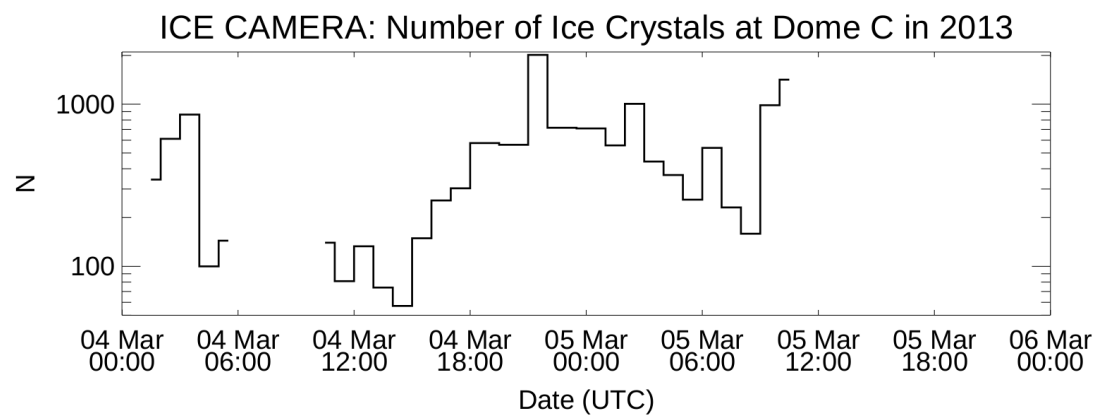
Fig. 8: Time evolution of the number of ice crystals measured by the ICE-CAMERA integrated

over one hour from 4 to 5 March 2013 above the Dome C station.

885

886

887

888
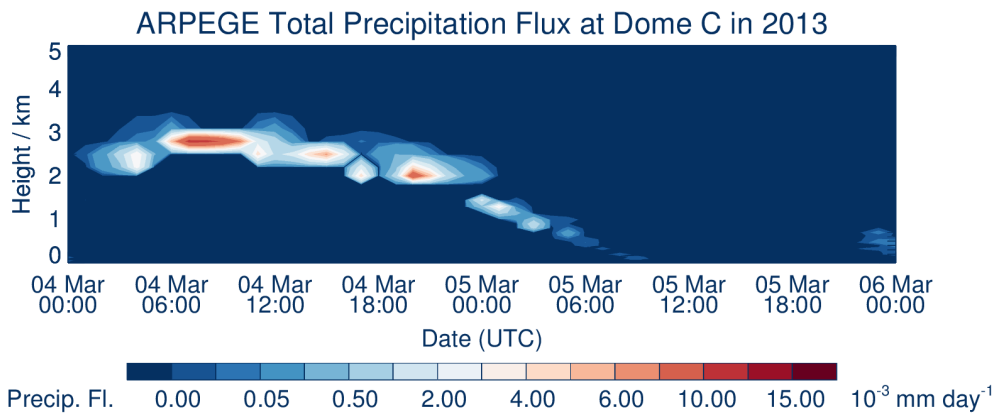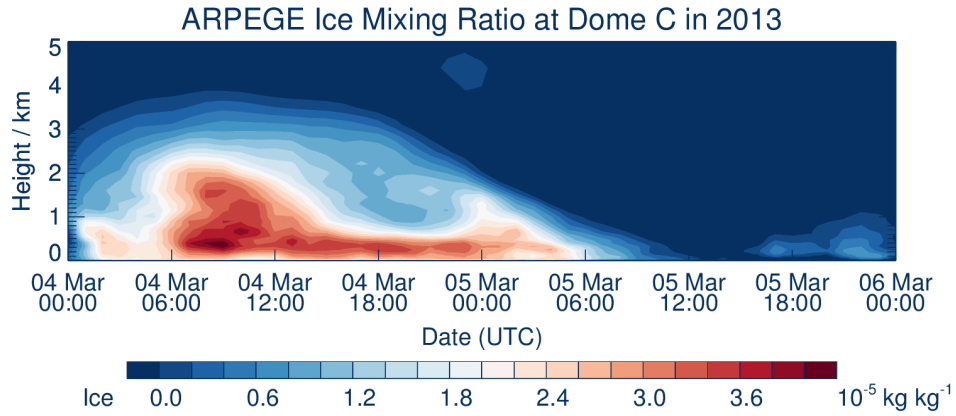
Fig. 9: Time evolution of the Ice Water Mixing ratio (top) and of the Total Precipitation Flux

890 (bottom) from 4 to 5 March 2013 above the Dome C station as calculated by the ARPEGE

891 model.

892

893

894
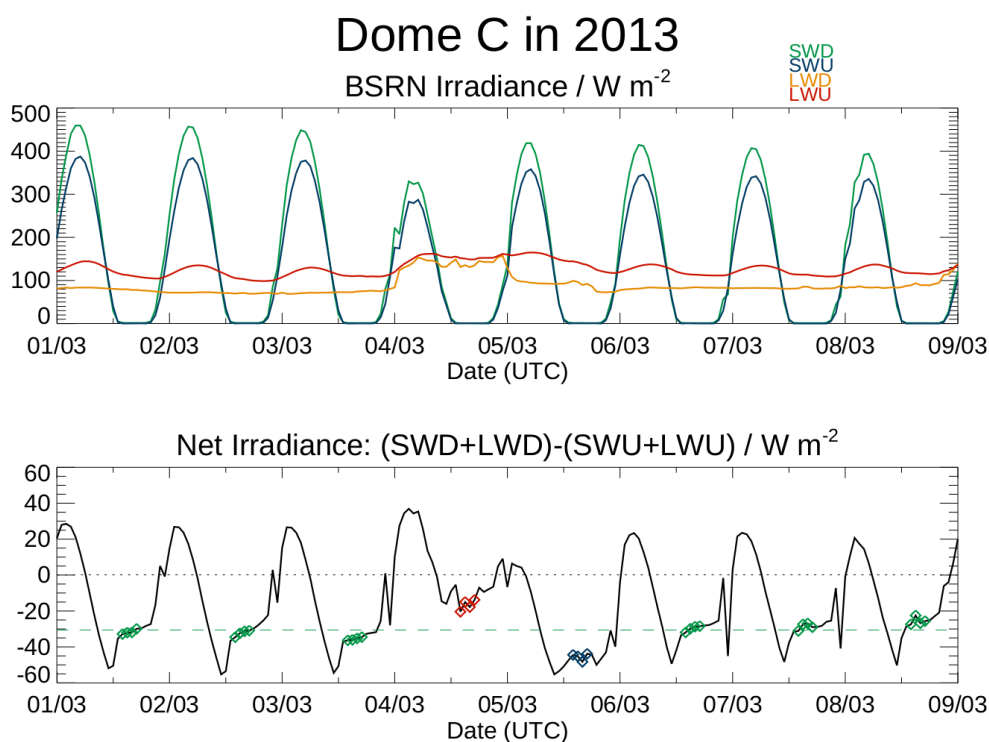
895 **Fig. 10:** (Top) Time evolution of downward shortwave radiation (SWD, green line), upward

896 shortwave radiation (SWU, blue line), downward longwave radiation (LWD, orange line), and

897 upward longwave radiation (LWU, red line) from 1 to 9 March 2013 above Dome C as

898 measured by the BSRN instruments. (Bottom) Net irradiance (SWD+LWD-SWU-LWU) as

899 measured by the BSRN instruments. The horizontal green dashed line represents the net

900 irradiance averaged between 14:00 and 17:00 UTC (represented by green diamonds) from 1 to

901 8 March excluding 4 and 5 March. The red and blue diamonds represent the net irradiances

902 measured between 14:00 and 17:00 UTC on 4 March (thick cloud episode) and 5 March

903 (diamond dust/ice fog episode), respectively.

904

905

906

907

908
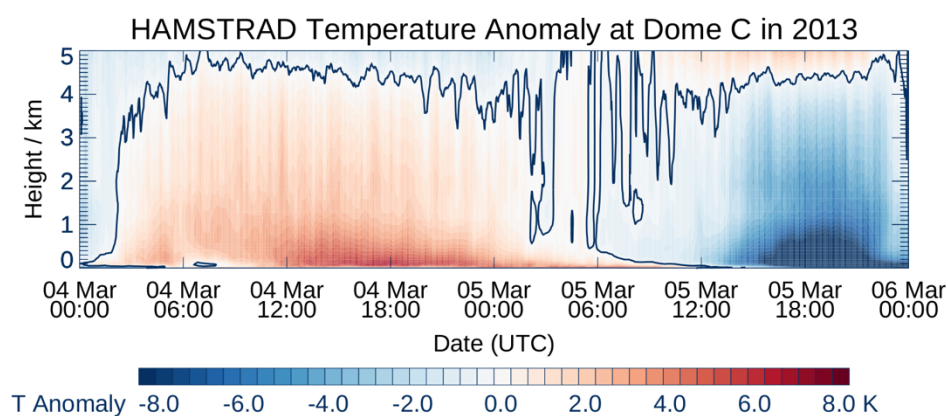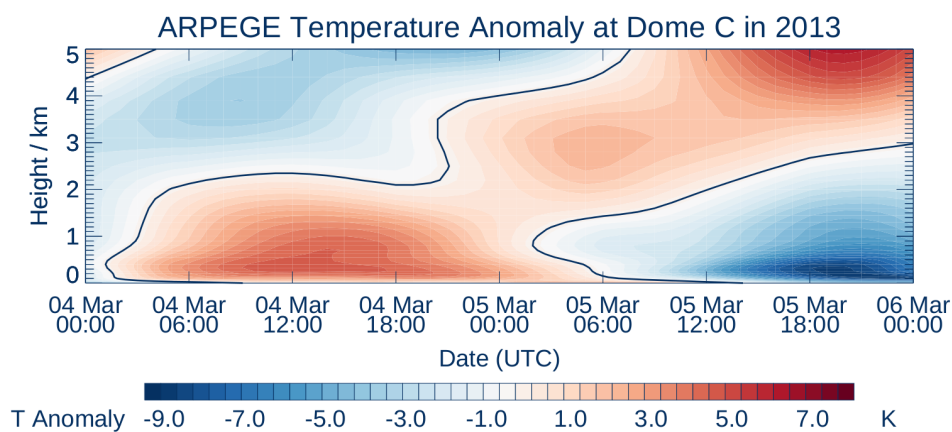
909 **Fig. 11:** Temperature anomaly from 4 to 5 March 2013 above the Dome C station as calculated

910 by the ARPEGE model (top) and as measured by the HAMSTRAD radiometer (bottom).

911

912

913
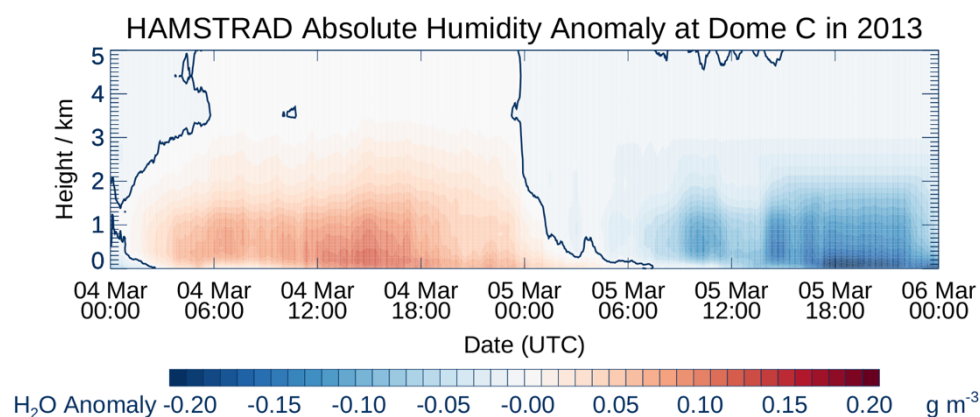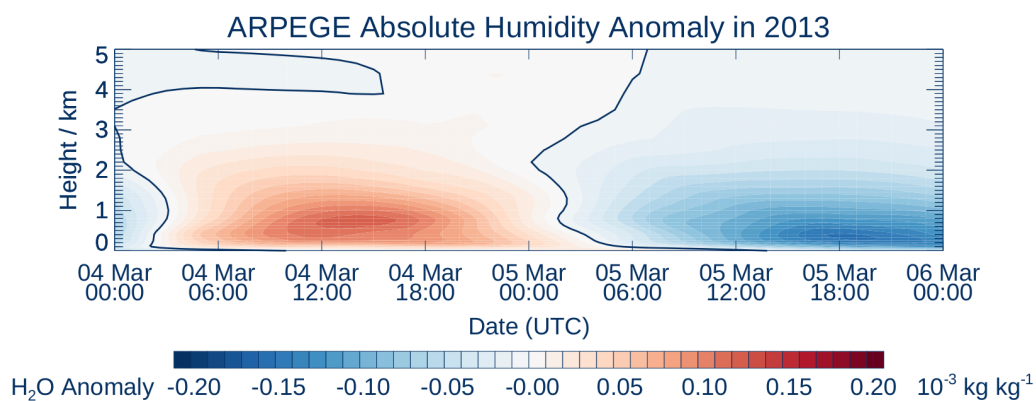
914 **Fig. 12**: Absolute Humidity anomaly from 4 to 5 March 2013 above the Dome C station as

915 calculated by the ARPEGE model (top) and as measured by the HAMSTRAD radiometer

916 (bottom).

917

918

919
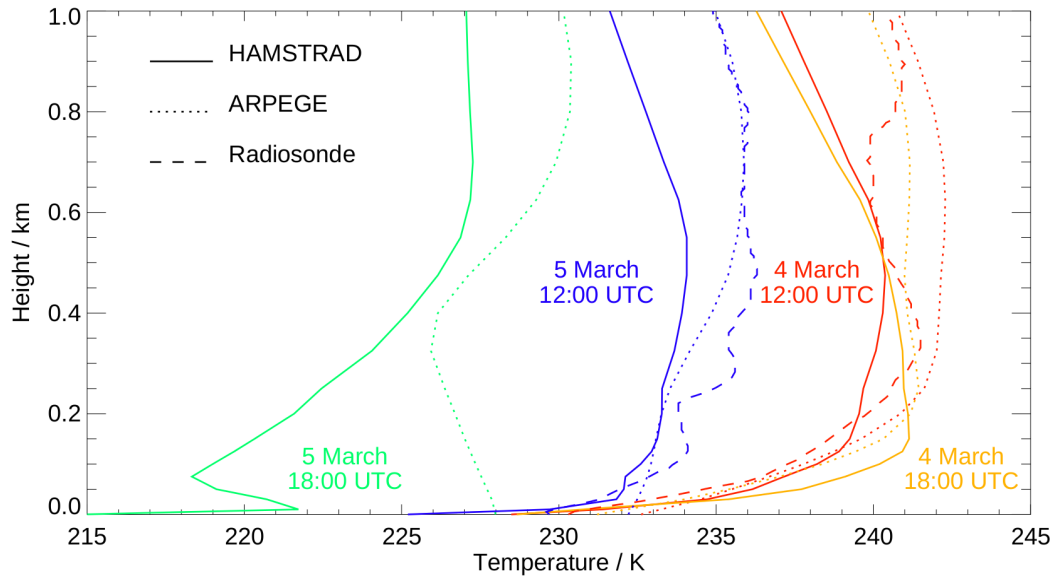
Fig. 13: Vertical distribution of temperature measured by HAMSTRAD (solid line), and radiosondes (dashed lines) and calculated by ARPEGE (dotted lines) on 4 March 12:00 UTC (red line) and 18:00 UTC (orange line) and on 5 March 12:00 UTC (blue line) and 18:00 UTC (green line). Note radiosondes are only available at 12:00 UTC.

924

925

926
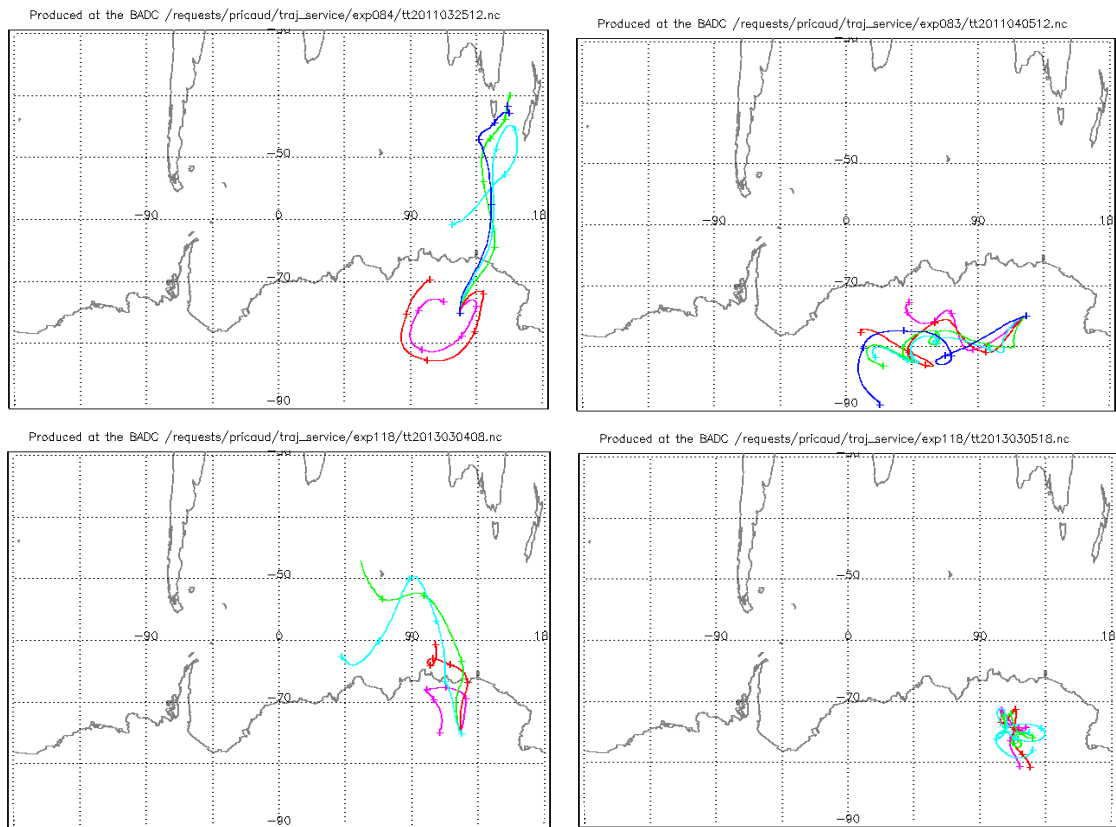
927
928
929
930
931 **Fig. 14:** (Top) Five-day back-trajectories of air masses originated from Dome C on 25 March

932 2011 at 12:00 UTC (left) and on 5 April 2011 at 12:00 UTC (right) at 650 (pink line), 600 (red

933 line), 500 (green line), 400 (light blue line) and 300 hPa (dark blue line). (Bottom) Same as top

934 but on 4 March 2013 at 08:00 UTC (left) and on 5 March 2013 at 18:00 UTC (right).

935
936

937

938
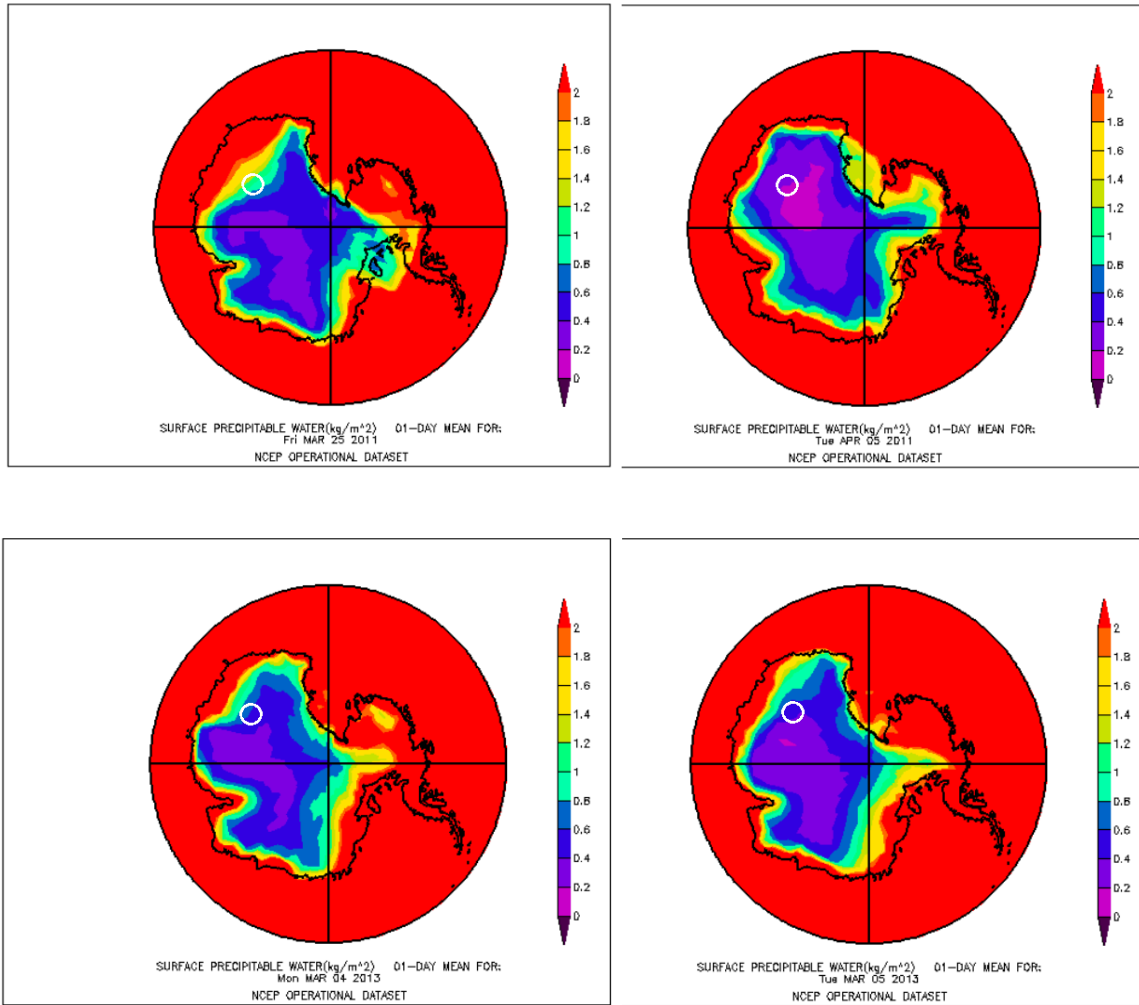
939 **Fig. 15:** IWV calculated above the Antarctic continent from the NCEP/NCAR operational

940 analyses on 25 March 2011 (top left), 5 April 2011 (top right), 4 March 2013 (bottom left) and

941 5 March 2013 (bottom right). The white circle represents the position of the Dome C station.

942

943

944
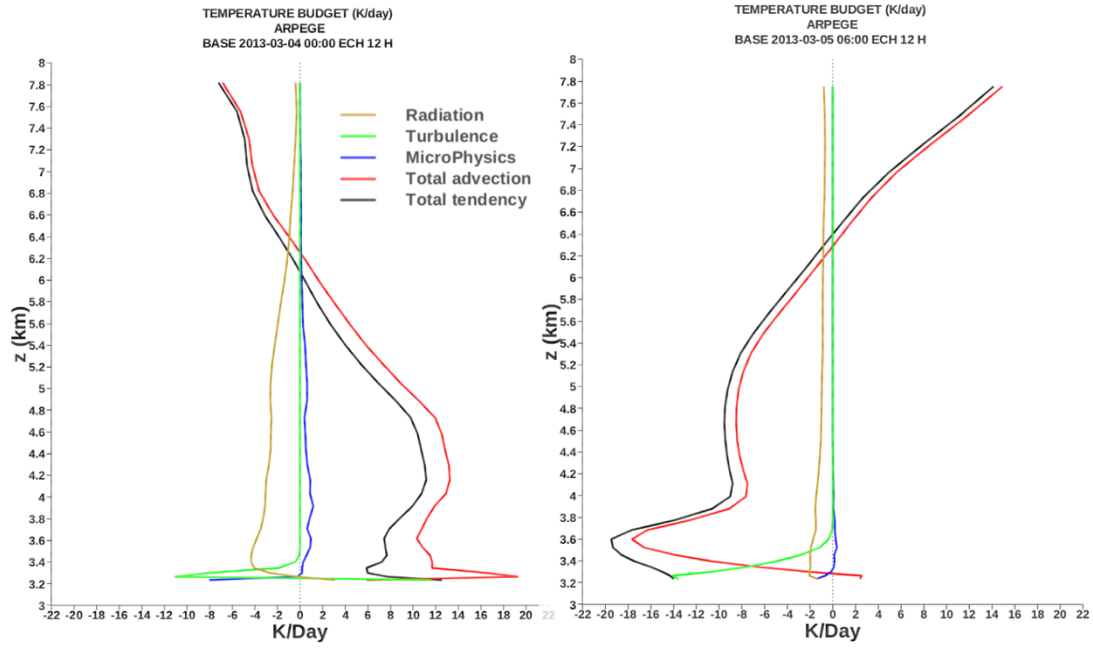
945 **Fig. 16:** (Left) Temperature budget calculated by ARPEGE on 4 March 2013 over the 12-h

946 period 00:00-12:00 UTC induced by radiation (brown), turbulence (green), microphysics

947 (blue), total advection (red) showing the total tendency (black). (Right) Same as Left but on 5

948 March 2013 over the 12-h period 06:00-18:00 UTC.

949

950
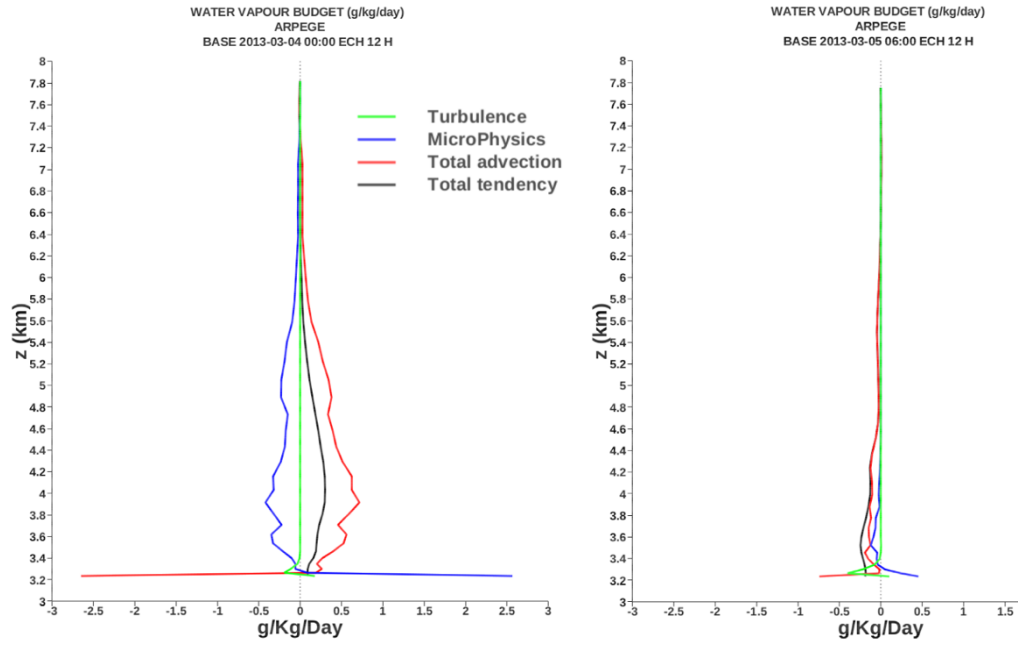
951 **Fig. 17:** (Left) Water vapour budget calculated by ARPEGE on 4 March 2013 over the 12-h

952 period 00:00-12:00 UTC induced by turbulence (green), microphysics (blue), total advection

953 (red) showing the total tendency (black). (Right) Same as Left but on 5 March 2013 over the

954 12-h period 06:00-18:00 UTC.

955

956